Modulating the Fe–N 4 Active Site Content by Nitrogen Source in Fe–N–C Aerogel Catalysts for Proton Exchange Membrane Fuel Cell

Hongxin Ge, Nicolas Bibent, Keyla Teixeira Santos, Kavita Kumar, Julien Jaxel, Moulay-Tahar Sougrati, Andrea Zitolo, Marc Dupont, Frédéric Lecoeur, Michel Mermoux, et al.

Modulating the Fe-N_4 active sites content by nitrogen source in Fe-N-C aerogel catalysts for Proton Exchange Membrane Fuel Cell

Hongxin Ge (a), Nicolas Bibent (b), Keyla Teixeira Santos (c), Kavita Kumar (c), Julien Jaxel (a), Moulay-Tahar Sougrati (b), Andrea Zitolo (d), Marc Dupont (b), Frédéric Lecoeur (b), Michel Mermoux (c), Vincent Martin (c), Laetitia Dubau (c), Frédéric Jaouen (b), Frédéric Maillard (c), Sandrine Berthon-Fabry (a*)

(a) MINES ParisTech, PSL University PERSEE - Centre procédés, énergies renouvelables et systèmes énergétiques, CS 10207 rue Claude Daunesse F-06904 Sophia Antipolis Cedex, France.

(b) ICGM, Univ. Montpellier, CNRS, ENSCM, 1919 route de Mende, 34293 Montpellier, France

(c) Univ. Grenoble Alpes, Univ. Savoie Mont Blanc, CNRS, Grenoble INP, LEPMI, 38000 Grenoble, France

(d) Synchrotron SOLEIL, L'orme des Merisiers, BP 48 Saint Aubin, 91192 Gif-sur-Yvette, France.

*Corresponding author.

E-mail address: sandrine.berthon-fabry@mines-paristech.fr (S. Berthon-Fabry). Tel: +33 493957547

Fax: +33 493957535

Abstract

Fe-N-C material is regarded a promising non-precious-metal catalyst for oxygen reduction reaction (ORR) to replace Pt-based catalysts, but its activity and mass transport remain problematic before a large scale application in proton exchange membrane fuel cells (PEMFCs). Our previous research developed an Fe-N-C aerogel catalyst by pyrolyzing resorcinol-melamine-formaldehyde (RMF) aerogel containing iron precursors. The abundance of micro and mesopores in aerogel is known to improve the mass-transport properties of Fe-N-C cathodes in PEMFC, facilitating the diffusion of O_2 to the Fe-N_4 sites. Herein, to further improve the ORR activity while maintaining good mass transport properties, a series of Fe-N-C aerogel catalysts was synthesized by modulating the nitrogen source (melamine) content and the texture in the RMF aerogel precursor. The Fe content in catalysts presents a positive relationship with melamine content in the aerogel, with adequate texture, indicating the important function of nitrogen source in stabilizing Fe atoms during pyrolysis to form Fe-N_4 active sites. ^{57}Fe Mössbauer spectroscopy revealed a majority of O-Fe(III)N_4C_{12} configuration of the active sites, which is consistent with the variation of pyrrolic N content with Fe derived from X-ray photoelectron spectroscopy. As a result, the mass activity of the series of catalysts exhibits a linear relationship with Fe content and reaches to 3.0 A g^{-1} at 0.8 V vs RHE in 0.05 M H_2SO_4 and rotating disk electrode (RDE) setup. Their performance in PEMFC exhibits same tendency with the RDE setup. In addition, the H_2/air PEMFC polarization curves do not show any diffusion-limited current density effects, even at 0.7 A cm^{-2} with a cathode based on a Fe-N-C catalyst prepared with high melamine content. This work reveals the importance of nitrogen source to reach high atomically dispersed Fe content in Fe-N-C catalysts with low yield of Fe nanoparticles and mass transport properties in PEMFC are not affected by low mesopore volume for aerogel-based catalysts.

Key words: Non-precious metal catalyst, Fe-N-C catalyst, carbon aerogel, oxygen reduction reaction, PEMFCs

Graphical abstract

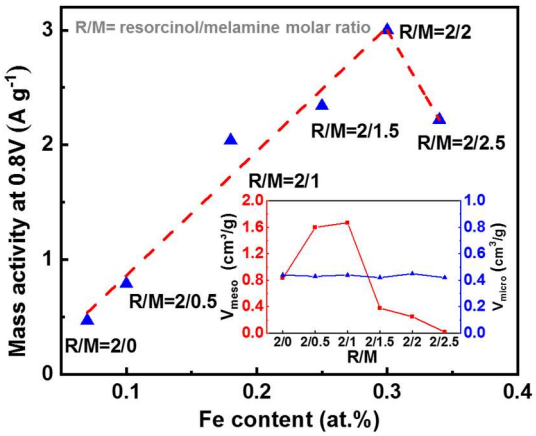

1 Introduction

Climate change is a global emergency that goes beyond national borders. To substantially reduce global greenhouse gas emissions, renewable energies, such as wind, solar, and tide should play a key role. However, due to the intrinsically intermittent power generation of these renewable energies, it is necessary to convert them with an intermediate carrier that can generate power stably and sustainably. Herein, hydrogen (H_2) is a promising candidate as an energy vector, because it can be produced from renewable electricity by water electrolyzers,[1] stored for long periods,[2] and reconverted on demand to electric power in fuel cells, without any greenhouse gas emission.[3]

H_2/air proton exchange membrane fuel cell (PEMFC) is one of the most promising fuel cell types, especially for transport and portable power applications. However, due to the sluggish oxygen reduction reaction (ORR) on the cathode and the acidic environment of PEMFC, large quantities of platinum (Pt)-based electrocatalysts are necessary to reach the acceptable power performance of PEMFCs, which impedes their broader commercialization and threatens their sustainability.[4] Therefore, developing non-precious metal catalysts for the ORR in acid media is highly desirable. In the past decades, numerous materials have been widely investigated for ORR both in acid and/or alkaline media, such as metal oxides,[5–7] metal chalcogenides,[8–10] metal-free nanostructured carbon materials,[11,12] and especially transition metal-nitrogen-carbon (Me-N-C) catalysts.[13–18] Some of recently reported iron (Fe)-N-C catalysts present an initial ORR activity approaching that of platinum-based catalysts in rotating disk electrode (RDE) setup and in PEMFC.[19–23]

Me-N-C catalysts are typically synthesized by pyrolyzing precursors of metal, nitrogen, and carbon, and among them, Fe-N-C catalysts were found to be the most active.[14,15,24–26] Atomically dispersed Fe centers coordinated by pyridinic and/or pyrrolic nitrogen atoms (usually, four nitrogen atoms, Fe-N_4 site) are considered as the most active sites in Fe-N-C catalysts, such sites having likely different site-specific activity and stability depending on their detailed configuration, the local carbon matrix structure, and/or the type of pores that connects them to the electrolyte.[24,27–32] Therefore, the mass activity of Fe-N-C catalysts relates to the number of accessible Fe-N_4 sites per mass of catalyst (site density, SD) and the average ORR turnover frequency (TOF) of all accessible sites.[21] The TOF may change depending on the detailed structure of the Fe-N_xC_y sites,[18,26,27,30] the delocalization of electrons on the carbon surface, and the presence of highly basic N-groups on the surface.[33–35] Since the pathways to increase the TOF are limited, another way to enhance the mass activity of Fe-N-C catalysts is to increase the SD. This can be achieved either by increasing the absolute amount of atomically dispersed Fe or by increasing the fraction of Fe-N_4 sites that are accessible to O_2.[21] However, a straightforward increase of Fe content, without precaution or synthesis optimization, usually increases the yield of Fe clusters rather than Fe-N_4 sites. A large specific surface area (S_{BET}) of the carbon substrate can help to promote the atomic dispersion of Fe at high Fe contents.[16,18,36] To our knowledge, the most active Fe-N-C catalyst might be considered to be the one reported by Jiao *et al.*,[21] which was synthesized by chemical vapor deposition of Fe on a Zn-N-C substrate containing Zn-N_4 sites, itself derived from a sacrificial Zn-based metal organic framework (MOF). The interconnected alveolar nanostructure of the MOF-derived carbon leads to a large surface area and micropore volume while $FeCl_3$ vapor leads to a transmetallation event from Zn-N_4 to Fe-N_4 active sites, achieving an unprecedented high SD of 1.0×10^{20} sites g^{-1} (measured by nitrite stripping assuming 3 electron mechanism). On the other hand, mass transport properties are also important to improve fuel cell performance with Fe-N-C cathodes, because a thicker catalyst layer on the cathode is required with Fe-N-C compared to platinum-based catalysts, to compensate for their lower mass activity.[37] The design of micro-meso or micro-meso-macroporous structures can improve the mass transport properties of Fe-N-C cathodes, facilitating the diffusion of O_2 to the Fe-N_4 sites, the latter being often located in micropores.[38] For example, Atanassov *et al*. have developed a family of ordered micro-mesoporous Fe-N-C catalysts with the silica templating approach, that offers interesting mass-transport properties in H_2/air PEMFCs.[39–42] However, hydrofluoric acid is required to remove the silica template, which is extremely hazardous and environmentally unfriendly. The commercial Pajarito Powder non-precious-metal catalysts are also prepared in this way.

Carbon aerogels are promising candidates of carbonaceous substrate for large-scale preparation of Fe-N-C catalysts, owing to their high specific surface area, tunable pore size distribution, and high electrical conductivity.[12,43–47] Other types of carbon gels, including xerogels and cryogels, have comparatively low specific surface area and low pore volume due to the collapse of the gel skeleton during gel drying.[48,49] Supercritical drying is a desirable method to remove organic solvents from hydrogels without causing excessive stress on the solid network, preserving the highly porous structure of the obtained aerogel.[46] However, no highly active carbon aerogel-derived Fe-N-C catalysts in acidic media has been reported hitherto due to the lack of Fe-N_4 active sites.[50–54] Therefore, it is still a challenge to develop a practical method to prepare the Fe-N-C aerogel catalyst with both high content of Fe-N_4 active site and excellent mass transport properties. Elbaz *et al.* combined the advantages of the three-dimensional covalent organic framework and carbon aerogel in heat-treated iron porphyrin aerogels, which achieve both high surface area and density of active sites.[55–57]

Our group has previously synthesized Fe-N-C aerogels by pyrolyzing resorcinol-formaldehyde-melamine organic aerogel, where the impacts of iron precursor, process parameters, and heat treatment condition on the microstructure, composition, and ORR performance were carefully investigated.[58,59] Resorcinol (acronym R) and melamine (acronym M) are the sources of C and N respectively, and the Fe precursor was introduced during the polymerization step. Different from the post-introduction of N and Fe sources onto a pre-existing carbon substrate, the presence of well-dispersed N and Fe sources in the aerogel precursor can promote the formation of Fe-N_4 active sites and reduce the yield of Fe-rich nanoparticles during pyrolysis.[51,60] However, excessive M content can decrease the porosity of the aerogel and even impede the gelation process.[12,61]

Herein, a series of Fe-N-C catalysts were obtained and characterized by modulating the M content, in order to define the limits of the gelation parameters and to identify the relationships between the gelation parameters, materials' structure, porosity, activity, and mass-transport properties. The porosity and specific surface area of the catalysts were determined by nitrogen (N_2) sorption. The nitrogen composition was studied by X-ray photoelectron spectroscopy (XPS), and the Fe content was determined by inductively coupled plasma mass spectrometry (ICP-MS). The coordination environment of Fe was investigated by X-ray absorption spectroscopy (XAS) and ^{57}Fe Mössbauer spectroscopy. With the present synthesis approach, we found that increasing the amount of M is crucial for increasing both the N and Fe content, promoting the formation of Fe-N_4 sites and therefore the activity of the catalysts, as measured in RDE and in PEMFC. The M content also modifies in a

non-linear way the mesopore volume, leading to a series of materials with various pore size distributions. No positive correlation was however found between mesopore volume and mass-transport properties, as examined with H_2/air PEMFC tests. The optimized catalyst in this work was obtained with a R/M molar ratio of 2/2, featuring Fe mainly as Fe-N_4 sites with a D1 quadrupole doublet Mössbauer signature, assigned to high spin Fe(III)-N_4 site. The optimized catalyst outperforms a commercial Fe-N-C catalyst from Pajarito Powder, selected as a comparison, in H_2/air PEMFC test.

2 Experimental methods

Catalyst synthesis

The Fe-N-C catalysts were prepared according to a protocol adapted from earlier works.[58,59] Resorcinol (99%, Alfa Aesar), formaldehyde (acronym Fo, 37wt% solution, Acros Organics), melamine (99%, Acros Organics), and anhydrous $FeCl_3$ (98%, Acros Organics) were used as received. All these precursors were mixed with defined ratios (see below) in distilled water, together with anhydrous sodium carbonate (acronym NaC, 99.9999%, Fluka) as the catalyst to promote polymerization. The M content was modulated according to the molar ratio of R/M at the aerogel preparation stage. The reactants and solvent were stirred at 70 °C with the molar ratio of 2:(4+3x):x for R:Fo:M, where x is the relative molar content of M. The catalyst content was kept at a molar ratio of R:NaC=2:0.033, and the solid content of (R+M+Fo) was controlled to 20% by adapting the content of water. $FeCl_3$ was added after 30 min polymerization. The molar ratio (R+M):Fe was kept constant with a value of 1:0.01, targeting *ca.* 1 wt. % Fe in the final catalysts by assuming no iron was removed during the acid leaching step and around 70% mass loss of (R+M+F) after pyrolysis based on our pre-experimental work.[58,59] The specific quantities of products were listed in **Table S1**. Subsequently, the pH of solution was adjusted to 8 by adding NaOH solution (2 M) under continuous stirring until gel formation. The hydrogel was then cured in a water bath at 70 °C for 120 h. The obtained hydrogels were subjected to a water-acetone exchange 3 times per day, for 3 days, followed by CO_2 supercritical drying to preserve the nanostructured porosity. Subsequently, the organic aerogels were cut into small pieces and then pyrolyzed at 800 °C under N_2 flow for 1 h. The tube furnace was heated with a ramp rate of 4 °C min^{-1} and maintained for 1 h at 800°C. Afterward, the furnace was turned off to cool down to room temperature. The N_2 flux was kept on during the whole process.

The carbonized aerogel pieces were sealed in a zirconium-oxide pot of 50 mL with balls of the same material, and subjected to ball-milling with machine Retsch S100. In detail, the mass ratio of balls to sample was kept at 30:1. The large pieces were pre-ground with 10 mm diameter balls at 400 rpm for

15 min, and further ground with 5 mm diameter balls at 400 rpm for 60 min. The obtained powders were washed at 80°C with 0.5 M H_2SO_4 for 7 h in a refluxing device to remove Fe particles or other acid-unstable Fe species generated during pyrolysis. The acid-washed powder was then subjected to a second heat treatment at 950°C under a diluted NH_3 (10% NH_3 + 90% N_2) atmosphere. The furnace was heated with a ramp rate of 4 °C min^{-1} until 950°C under N_2 and then switched to diluted NH_3. After holding at 950 °C for 45 min under diluted NH_3, the gas was switched back to pure N_2 and turned off the furnace. The samples were let to cool down to room temperature under N_2 flux. The final catalysts are labeled as $FeCl_3$-R/M=2/x, where x is the relative molar amount of M, as described previously in the synthesis protocol.

Physicochemical characterization

The morphologies of the catalysts were determined by scanning electron microscopy (SEM) (MAIA) operated at 3.0 kV. Transmission electron microscopy (TEM) and energy dispersive X-ray spectroscopy (X-EDS) were used to differentiate the carbon morphologies and the local Fe content of the different materials, respectively. A JEOL 2010 TEM operated at 200 kV with a resolution of 0.19 nm was used. At least five different catalyst regions of the TEM grids were analyzed by X-EDS. Nitrogen sorption isotherms were measured at -196°C with a Micromeritics ASAP 2020 instrument, after degassing the samples under 10 mmHg at 200 °C for 8.3 hours. S_{BET} was determined via the Brunauer–Emmett–Teller (BET) equation while the total pore volume (V_t) was estimated from the adsorption isotherm at the relative pressure of 0.995. The pore size distribution (PSD) was calculated using the 2D-NLDFT-Heterogeneous Surface method based on the adsorption isotherms. The micropore volume (V_{micro}) and mesopore volume (V_{meso}) were obtained from the PSD analysis. The cross-linking degree of the aerogel before pyrolysis was investigated by attenuated total reflection Fourier transform infrared (ATR-FTIR) spectroscopy. The measurements were performed in the range of 4000-600 cm^{-1} on a Bruker Tensor 27 machine using OPUS 7.8 software. X-ray photoelectron spectroscopy (XPS) was used to identify the elemental composition of the surface of the catalysts. The measurements were performed using Thermo ScientificTM K-AlphaTM spectrometer equipped with an Al Kα1,2 monochromatic source (1486.6 eV). All samples were analyzed with a spot size of 200 μm and repetitive tests were conducted on four different spots of all samples to ensure the accuracy of the measurements. A survey spectrum and higher resolution multiplex scan spectra (C 1s, O 1s, N 1s, and Fe 2p core levels) were obtained and analyzed by Avantage. For the fitting, the peaks were constrained to have a full width at half-maximum between 1.2 and 1.4 eV, and the peak positions were identified by fixing their difference of binding energy to pyridinic N at 398.8 eV.[62–64] The global Fe content in the catalysts was determined by inductively

coupled plasma mass spectrometry (ICP-MS). A PerkinElmer NexION 2000c instrument was used. Daily prepared iron (^{56}Fe) solutions were used for the calibration curves. Five solutions were prepared from commercial standard mono-element ICP-MS solution (Carl Roth GmbH & co. KG, 1000 mg L^{-1}) in order to obtain five-point calibration curves at 0, 2, 5, 10, and 20 µg L^{-1}. Rhodium (^{103}Rh) was used as the internal standard. To avoid any polyatomic interferences, the helium collision mode was used. X-ray diffraction (XRD) analysis was performed using an X"pert Pro Philips diffractometer using filtered Cu Kα radiation (λ=0.15418 nm) generated at 40 kV and 30 mA. The diffraction angles of the diffraction peaks were determined with High score software. The average values of perpendicular graphene layers (L_c) and their interlayer spacing (d_{002}) were calculated from the Debye-Scherrer equation.

Raman spectroscopy was used to differentiate the carbon structure of the different electrocatalysts. A Renishaw InVia instrument in a backscattering configuration (with 532 nm as excitation) was used for each measurement. An objective focus of X50 was used to collect the scattered radiation. In order to prevent the excess heating or probable degradation of the samples under the laser beam, the spectrometer was used in a 'line mode' with low incident power densities (~50 µW/µm^2). LabSpec 5.0 software was used for fitting the Raman spectra and five bands were considered, as our previous work.[65] The average values of in-plane graphite crystallite size (L_a) was calculated from the Knight and White equation:[66]

$$L_a(nm) = 4.4\ (\frac{I_{D1}}{I_G})^{-1} \qquad \text{(Equation 1)}$$

The ^{57}Fe Mössbauer spectra (Wissel, Germany) were acquired in transmission mode. The source was ^{57}Co: Rh. The velocity driver was operated in constant acceleration mode with a triangular velocity waveform, and the velocity scale was calibrated with the magnetically split sextet of a high-purity α-Fe foil at room temperature. A mass of *ca.* 200 mg of catalyst was mounted in a 2 cm^2 holder. Mössbauer measurements were performed at -268°C with a helium flow cryostat (SHI-850 Series from Janis, USA). The spectra were analyzed by fitting the experimental spectrum with an appropriate combination of quadrupole doublets and sextets with Lorentzian profiles.

Fe K-edge XAS were collected at room temperature at SAMBA beamline (Synchrotron SOLEIL, Saint-Aubin, France). The beamline is equipped with a sagittally focusing Si 220 monochromator, and X-ray harmonics are removed by two Pd-coated mirrors. The catalyst powders were pelletized as disks of 10 mm diameter with 1 mm thickness, using Teflon powder (1 µm particle size) as a binder. Measurements were carried out in transmission or fluorescence mode, depending on the iron content.

Electrochemical measurements

RDE measurements were performed under atmospheric pressure and room temperature in a three-electrode cell with a potentiostat/galvanostat from Bio-Logic (HCP-803). The reference electrode was a reversible hydrogen electrode (RHE) and the counter electrode was a graphite electrode. The catalyst ink was prepared by ultra-sonicating 10 mg catalyst powder, 95 µL 5 wt. % Nafion D-520, 752 µL ethanol, and 46 µL deionized water for 1 h. 7 µL of this ink was dropped on a 0.196 cm^2 glassy carbon disk, resulting in a catalyst loading of 0.4 $mg_{Fe\text{-}N\text{-}C}/cm^2$. The ORR activities were measured in an O_2-saturated 0.05 M H_2SO_4 aqueous solution. Linear scan voltammograms were recorded (LSV) at 10 mV s^{-1} from 1.1 to 0 V *vs*. RHE under constant revolution rate (1600 rpm). The same test was repeated in N_2-saturated electrolyte to eliminate the pseudo-capacitive current ('background' current). All obtained data were corrected for Ohmic-drop (iR-drop). Cyclic voltammograms between 0 and 1.0 V *vs*. RHE were measured at 10 mV s^{-1} in N_2-saturated electrolyte. The kinetic current densities of all catalysts were defined by the Koutecky-Levich equation as shown in Equation 2.

$$\frac{1}{j_k} = \frac{1}{j_F} - \frac{1}{j_{lim}} \quad \text{(Equation 2)}$$

where j_k, j_F *and* j_{lim} represent the kinetic current density (mA cm^{-2}), Faradic current density (mA cm^{-2}) and limiting current density (mA cm^{-2}), respectively.

The mass activity (A g^{-1}) was calculated as follows (Equation 3):

$$j_M = -\frac{j_k}{m} \quad \text{(Equation 3)}$$

where j_M (defined > 0) is the mass activity, and m is the catalyst loading (0.4 mg cm^{-2}) on the working electrode.

To determine the SD and TOF values, the nitrite adsorption and stripping analysis were realized through the method first introduced by Malko *et al* using 0.125 M $NaNO_2$ aqueous solution and a loading of 0.3 $mg_{Fe\text{-}N\text{-}C}/cm^2$. The nitrite stripping was recorded in a potential range of 0.2 to -0.2 V *vs*. RHE in an acetate buffer 0.5 M pH 5.2 solution.[67] ORR polarization curves were carried out at 5 mV/s and at 1600 rpm and were recorded for the unpoisoned, poisoned and recovered catalysts surface. The SD and TOF values were determined using the following equations:

$$SD(g^{-1}) = \frac{Q_{strip}(C\ g^{-1})\ N_A(mol^{-1})}{n_{strip}\ \ F\ (C\ mol^{-1})} \quad \text{(Equation 4)}$$

$$TOF(s^{-1}) = \frac{MA_{0.8}\ at\ pH\ 1\ (A\ g^{-1})\ N_A(mol^{-1})}{SD\ (g^{-1}) \times F\ (C\ mol^{-1})} \quad \text{(Equation 5)}$$

Where Q_{strip} is the excess coulometric charge associated with the reduction of one adsorbed nitrite ligand per site and n_{strip} is the number of electrons associated with this stripping. F and NA are the Faraday and Avogadro constants, respectively. $MA_{0.8}$ is the mass activity measured at 0.8 V *vs.* RHE

at pH = 1. In this work, the SD values were calculated considering a 3 electrons process for the reduction reaction with the formation of NH_3OH^+.[68]

For PEMFC measurements, the ink formulation applied to all Fe-N-C catalysts was 20 mg of catalyst, 915 µL of 5 wt.% Nafion solution (1100 EW Nafion, Sigma Aldrich), 63 µL of 1-propanol (>99.9% purity, Sigma Aldrich), and 272 µL of deionized water. The reagents were mixed and subjected to sonication for 1 hour. The ink was deposited on a 4.84 cm^2 gas diffusion layer (Sigracet 29-BC from Baltic Fuel Cells), depositing 210 µL aliquot of the ink each time followed by drying, and repeating this process until the total ink volume was deposited, resulting in a catalyst loading of 4.1 mg cm^{-2}. This ink formulation corresponds to a mass ratio of dry Nafion to catalyst (N/C) of 2. The effect of N/C was investigated in detail for the catalyst $FeCl_3$-R/M=2/1, and also for the commercial Fe-N-C catalyst from Pajarito Powder. The cathode was then dried at 80 °C, and hot-pressed at 135 °C with a Pt/C anode and a Nafion membrane (Nafion NR-211). The anode used for all PEMFC tests was 0.5 mg_{Pt} cm^{-2} on Sigracet 28-BC. PEMFC measurements were performed with a single-cell fuel cell with a serpentine flow field (Fuel Cell Technologies) using an in-house test bench and a Biologic potentiostat with a 50 A load and EC-Lab software. For H_2/O_2 PEMFC measurements, the temperature of the cell was 80 °C, the backpressure was 1 bar on each side, the flow rate was 150 mL min^{-1} on each side, and the relative humidity 100% was on each side. The conditions were the same for H_2/air measurements, except for the flow rate on the cathode side, which was increased to 480 mL min^{-1} of synthetic air (Air Liquide). Polarization curves were recorded by scanning the voltage at 1 mV s^{-1}.

3 Results and Discussion

Physico-chemical characterizations of catalyst precursors and catalysts

Figure 1 shows the FTIR spectra of the Fe-doped aerogels before pyrolysis, which constitute the precursors of the Fe-N-C catalysts, prepared with R/M ratio varying from 2/0 to 2/2.5. The assignment of absorption bands is listed in **Table S2**. For $FeCl_3$-R/M=2/0 (no melamine), the FTIR spectrum is similar to that of an aerogel prepared only from resorcinol and formaldehyde (RF seen in **Figure 1**), without $FeCl_3$. The absorption band at 1479 cm^{-1} belongs to the CH_2 scissor vibrations (from the condensation of the hydroxymethyl derivatives created in the resorcinol formaldehyde reaction), and the absorption band at 1614 cm^{-1} corresponds to benzene ring stretching vibrations.[69–71] The two absorption bands at 1222 and 1092 cm^{-1} are associated with C-O-C asymmetric/symmetric stretching vibrations of methylene ether bridges, which have been previously identified in the FTIR spectra of

RF aerogels.[69,71] This bond demonstrates the existence of benzylether structure which is typically derived from the polycondensation between methylol and resorcinol in basic condition.[43,46] With increasing melamine content, the absorptions derived from MF aerogel become more intense. Two sharp absorption bands at 1544 and 810 cm^{-1} can be unambiguously assigned to vibration modes that are specific to the triazine ring of melamine.[72] The relatively broad absorption band at 1350 cm^{-1} can be assigned to the stretching vibration of C-N bond between aromatic carbon and amine function.[72] An additional absorption band is visible at around 1000 cm^{-1}, which cannot be assigned to resorcinol-formaldehyde nor melamine-formaldehyde aerogel. It can instead be assigned to a N-CH_2-O stretching mode, indicative of crosslinking between resorcinol and melamine with methylene derived from formaldehyde as the linker.[73] The peak intensity increases with melamine content, indicating the proper integration of nitrogen atoms in the RMF aerogel backbone.

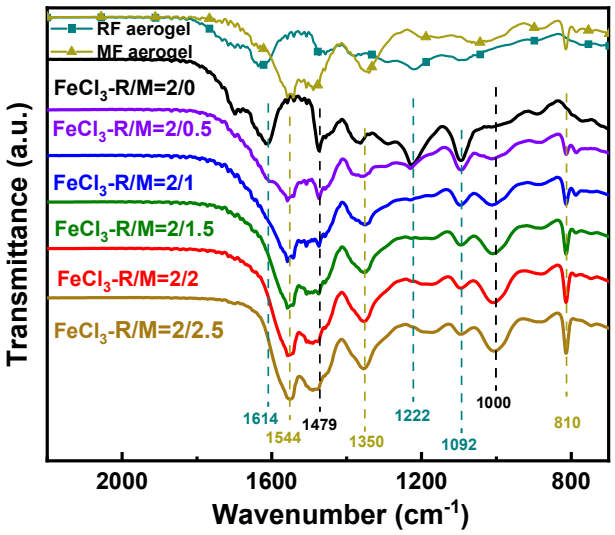

Figure 1. FTIR spectra of organic aerogel prepared with different R/M ratios.

All other characterizations were performed on the catalysts, *i.e.* after all synthetic steps, including the final thermal treatment in ammonia. Representative TEM images of the catalysts prepared with different melamine content are shown in **Figure 2**a-c and **Figure S1**a-c. The images reveal a change in the carbon matrix morphology between, on one hand, samples prepared with R/M ratios from 2/0 to 2/1.5, and, on the other hand, samples prepared with R/M ratios of 2/2 or 2/2.5. For the catalysts with low M content, typically $FeCl_3$-R/M=2/0.5, their TEM images show a highly porous texture, which is similar to those reported for RMF aerogel.[12,74] When R/M reaches 2/1.5, some pore-less platelets can be found, and finally, become the dominant morphology at R/M=2/2.5. A similar evolution can be observed in their SEM images as well (**Figure 2**d-f and **Figure S1**d-f). The catalysts

with low M content are formed by stacking spherical particles, indicating a high porosity as observed in TEM images. On increasing the M content, large and densely packed particles are observed, which implies a lower surface area and porosity.

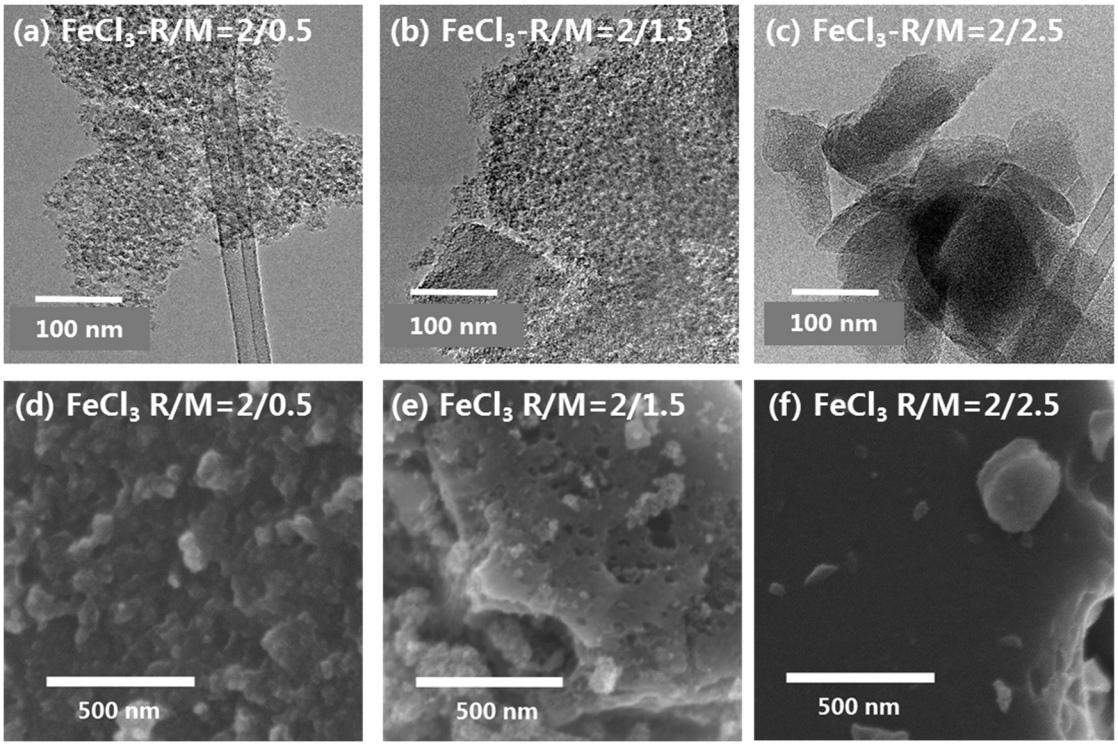

Figure 2. Carbon morphology of the catalysts prepared with R/M=2/0.5, 2/1.5, and 2/2.5. **(a)-(c)** TEM images and **(d)-(f)** SEM images.

The graphitic structure was further investigated with Raman spectroscopy and XRD. The XRD patterns and Raman spectra (**Figure S2**a and b) show that the carbon matrix is poorly organized for all R/M values, as indicated by their large peak width at 2θ=25.6º in XRD patterns, a peak assigned to the (002) diffraction of graphite, and as indicated by a high ratio of the *D* to *G* band intensities (I_D/I_G around 4.7) from Raman spectra.[34,75] The average values of in-plane graphite crystallite size (L_a) and the graphite crystallite thickness (L_c) were derived from I_D/I_G of Raman spectra and full width at half-maximum of the peak at 2θ=25.6º in XRD patterns (corresponding to d_{002}=0.36 nm), respectively (**Figure 3**a and b). An example of Raman fit is shown in **Figure S2**c. Both L_a and L_c values are lower at high melamine content, the decrease occurring when switching from R/M = 2/0.5 to R/M = 2/1. This indicates an increasing average structural disorder of the graphite matrix in the final catalysts with increasing melamine content at the aerogel preparation stage. The changes in L_a and L_c are however moderate, and the L_a values in particular are not commensurate with the size of the platelets seen by TEM for R/M values of 2/2 and 2/2.5, larger than 100 nm. These results indicate

that both the large platelets and highly porous texture are constructed by highly defective and/or nanometric units, whereas the decomposition of melamine leads to their different morphologies.[12]

Moreover, no Fe-rich particles can be observed from TEM images or identified from XRD patterns (**Figure 2**a-c and **Figure S2**b), suggesting that Fe exists as atomically dispersed Fe-N_4 sites.[18] However, nanometric particles of iron or iron oxides can be difficult to track with TEM or XRD, and Fe coordination was characterized by dedicated spectroscopies, as discussed later.

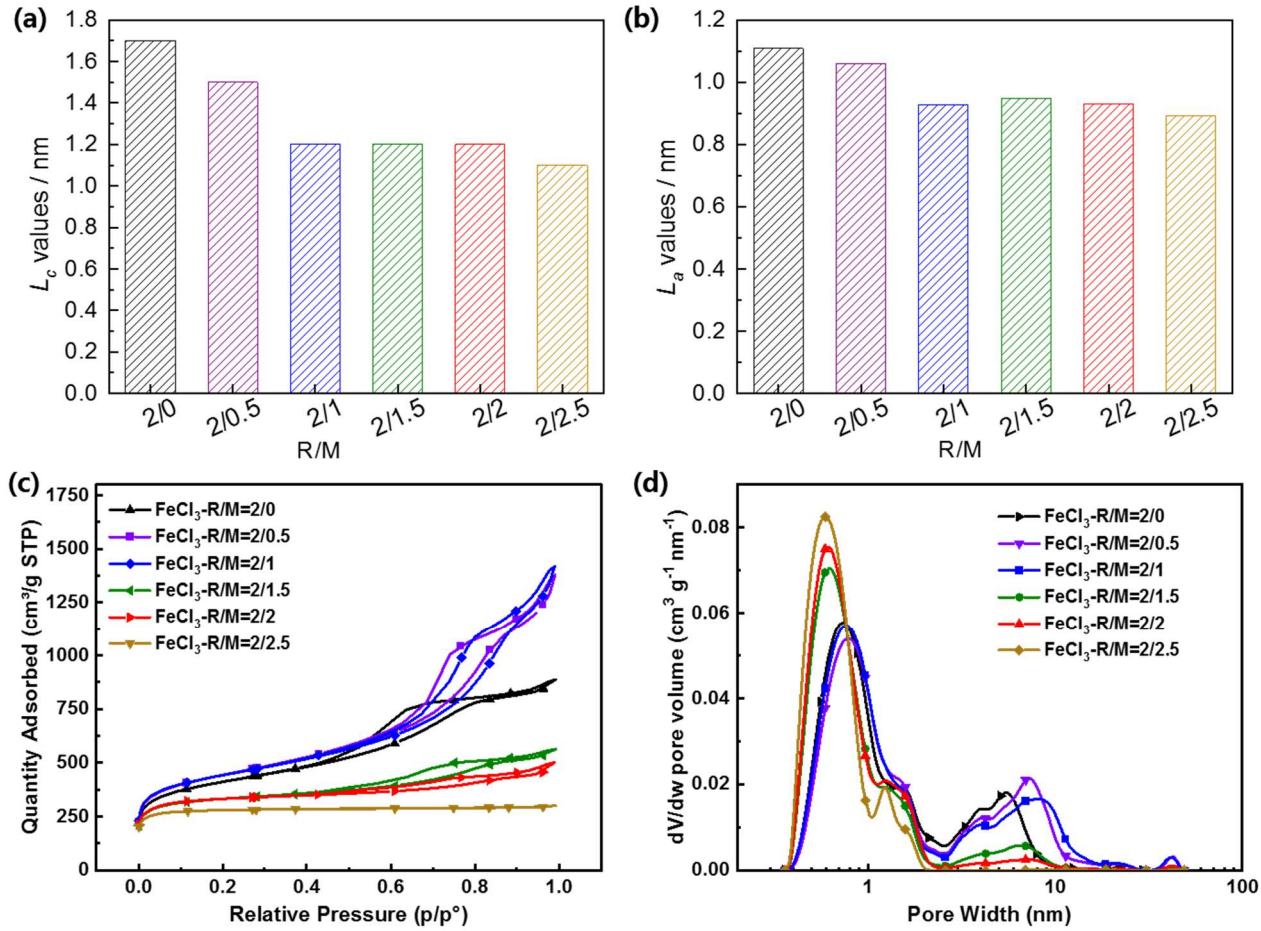

Figure 3. Structural and textural characterization of the catalysts prepared with different R/M ratios. (a) graphite crystalline thickness in the direction perpendicular to the graphene layers obtained from XRD, (b) in-plane graphite crystallite size obtained from Raman spectroscopy, (c) isotherms adsorption/desorption and (d) pore size distribution from N_2 adsorption isotherms at -196 ºC for the catalysts.

The lower mesoporosity in samples prepared with high melamine content is confirmed by N_2 sorption isotherms (**Figure 3**c, d and **Table 1**). The mesopore volume is slightly increased at R/M=2/0 to R/M=2/1, from 0.83 to 1.67 $cm^3\ g^{-1}$, then sharply decreased to only 0.02 $cm^3\ g^{-1}$ at R/M=2/2.5 (**Table**

1). The skeleton of hydrogel was constructed by linking the RF and MF units in the precursor solution and a part of the interspace between these units became the mesopores after drying and pyrolysis.[43,46] Different from thermally stable benzene rings in R, the triazine rings in M were decomposed during pyrolysis. At low M content, the evaporation of M decomposition products helps create more mesopores without destroying the skeleton of the aerogel. However, when this decomposition occurs in large numbers at high M content, it leads to a collapse of the aerogel texture, thus presenting more compact morphology and lower specific surface area and porosity.[47,74,76] In contrast to the mesopore volume, the micropore volume is almost constant with the R/M ratio, at 0.42-0.45 $cm^3\ g^{-1}$. The micropores are mainly formed by NH_3 etching of the carbon matrix, and the carbon atoms located on the edge of graphite particles are preferentially etched by ammonia compared to carbon atoms located in the plane of the graphite crystallites.[77] Since the melamine content weakly affects the average crystallite size of graphite after the first pyrolysis, the NH_3 etching degrees of carbon aerogels are similar and thus obtaining similar micropore volume.

In summary, all the catalysts in this series present a high specific surface area (>1000 $m^2\ g^{-1}$) and high micropore volume, which are usually considered necessary criteria to reach a high ORR activity with Fe-N-C catalysts. In addition, the hugely contrasting mesopore volume in this set of catalysts is useful to investigate the mass-transport properties in PEMFC and whether mesopores are important or not for high performance (discussed later).

Table 1. Surface and pore volume characteristics of Fe-N-C aerogel catalysts.

R/M	BET surface ($m^2\ g^{-1}$)	V_t ($cm^3\ g^{-1}$)	V_{micro} ($cm^3\ g^{-1}$)	V_{meso} ($cm^3\ g^{-1}$)
2/0	1481	1.37	0.44	0.83
2/0.5	1595	2.13	0.43	1.60
2/1	1596	2.20	0.44	1.67
2/1.5	1256	0.87	0.42	0.38
2/2	1271	0.78	0.45	0.25
2/2.5	1099	0.46	0.42	0.02

The chemical composition of the catalysts was investigated with ICP-MS and XPS. The bulk Fe content determined by ICP-MS increases dramatically with increasing melamine content (**Table 2**), even though the initial quantity of Fe precursor was kept at around 1 wt.% (with (R+M):Fe molar ratio kept constant) for all catalyst preparations. Two main hypotheses can explain this correlation. In the first one, the addition of melamine helps coordinate and disperse iron in the aerogel before pyrolysis, decreasing the amount of metallic iron or iron oxide particles formed during or after

pyrolysis, and therefore minimizing the amount of iron leached during the acid washing step. In the second hypothesis, the increasing amount of melamine leads to increasing mass loss of C and N as volatile products during pyrolysis, which indirectly increases the iron content in final catalysts. The very low Fe amount measured with R/M = 2/0 however supports that our first hypothesis is the main factor accounting for the Fe content in the final catalysts. Additionally, this hypothesis is supported by spectroscopic characterization of the iron environment in catalysts, as discussed later. The chemical composition was investigated by XPS (**Table 2**). The Fe content measured by XPS is similar to that measured with ICP-MS. While the N content also shows an increasing trend with increasing M, the relative increase is less than the increase in Fe content (**Table 2**). However, the N_{1s} narrow scan spectra identify a dramatic change in the type of N-groups present, the catalysts prepared with R/M = 2/0 showing a very weak signal at *ca.* 401 eV (pyrrolic N) while the relative intensity of this signal increases with the melamine content (**Figure 4**a).

To clarify the evolution of the type of N-species present as a function of the R/M synthesis parameter, the N 1s spectra were fitted with a set of six peaks assigned to different N-species, including nitrile at 398.0 eV, pyridinic N at 398.8 eV, coordinated N (Fe-N_x) or amine at 399.9 eV, pyrrolic N at 400.9 eV, quaternary N at 402.0 eV, and graphitic N at 403.3 eV, as listed in **Table 2**. An example of such a fit is given in **Figure S3**. **Figure 4**b presents the variation of the different N species with increasing M content. Notably, only the pyrrolic N content is positively correlated with the M content, whereas the other N-species are almost constant or only increase slightly with increasing M content. The molar ratio of pyrrolic N/Fe is close to 5.4 for the catalyst $FeCl_3$-R/M=2/0 then decreases with increasing M content to stabilize at around 4 until $FeCl_3$-R/M=2/1.5 (**Table 2**). This number corresponds well to the stoichiometry in Fe-N_4 sites, suggesting all nitrogen atoms involved in the ligation of Fe are of pyrrolic nature. The values are decreased to around 3 for $FeCl_3$-R/M=2/2 and $FeCl_3$-R/M=2/2.5, suggesting the existence of other Fe species.

Table 2. Chemical composition of the Fe-N-C aerogel catalysts.

R/M	ICP-MS Fe		XPS				Nitrile at%	Pyridinic at%	Fe-N_x (amine) at%	Pyrrolic at %	Quaternary at%	Graphitic at%	Pyrrolic/Fe
	wt.%	at.%	C at.%	N at.%	O at.%	Fe at.%	398.0 eV	398.8 eV	399.9 eV	400.9 eV	402.0 eV	403.3 eV	
2/0	0.33	0.07	95.57	2.94	1.39	0.10	1.05	0.50	0.45	0.54	0.28	0.12	5.4
2/0.5	0.49	0.10	95.22	3.00	1.63	0.16	0.94	0.55	0.43	0.61	0.35	0.13	3.8
2/1	0.85	0.18	93.69	3.21	2.89	0.22	0.84	0.52	0.52	0.78	0.38	0.18	3.5
2/1.5	1.17	0.25	94.32	3.44	1.97	0.27	0.79	0.52	0.45	1.00	0.46	0.22	3.7
2/2	1.36	0.30	93.54	3.76	2.32	0.36	0.94	0.57	0.50	1.14	0.43	0.18	3.2
2/2.5	1.54	0.34	92.91	4.17	2.49	0.43	1.01	0.66	0.53	1.30	0.48	0.19	3.0

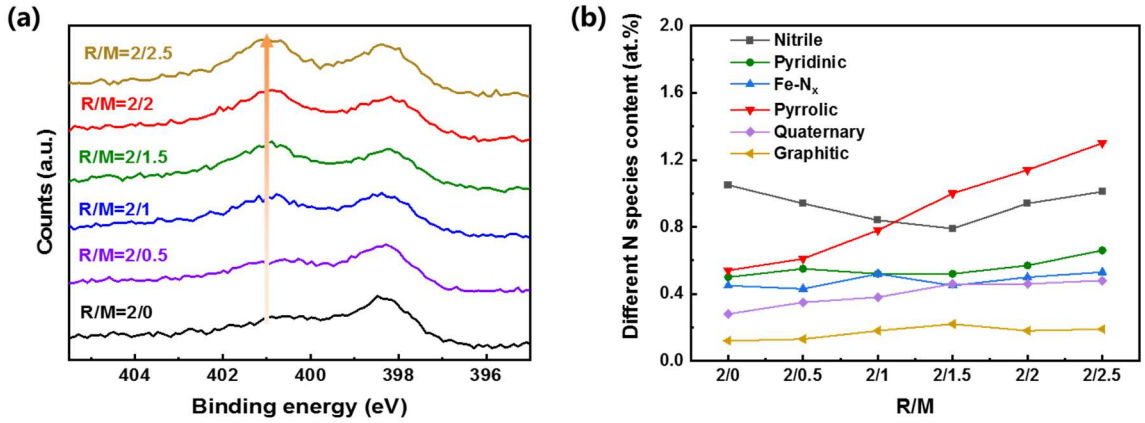

Figure 4. (a) N_{1s} XPS patterns, (b) evolution of different N species content with R/M.

Insights into the type of Fe species present were obtained from Fe K-edge XAS and ^{57}Fe Mössbauer spectroscopies. **Figure 5**a shows selected X-ray absorption near edge structure (XANES) spectra for three catalysts of the series, as well as the XANES spectrum of a reference Fe-N-C catalyst derived from ZIF-8 (labeled $Fe_{0.5}$) and for which Fe is known to be present as Fe-N_x active sites only.[27] The spectra show high similarities, suggesting Fe is mainly present as Fe-N_x coordination structures,[27,36] although the presence of nanometric iron oxides cannot be excluded due to similar XANES spectra with Fe-N_4 sites.[30] The Fourier-transformed EXAFS signals of down-selected catalysts (**Figure 5**b) are also similar to that of $Fe_{0.5}$, with the main signal at *ca* 1.5 Å, assigned to Fe-N or Fe-O bonds.[27,36,59,78] As for XANES, the presence of nanometric iron oxide cannot be excluded since the signal from Fe-N bonds in Fe-N_x sites and Fe-O from oxides cannot be distinguished, and the signal from Fe-Fe backscattering is not always discernible in nanometric oxides due to size and/or amorphous character of nano-oxides.[30] The iron coordination was further investigated with ^{57}Fe Mössbauer spectra collected at -268 ºC. The low-temperature acquisition enables distinguishing in particular nanometric iron oxides, contributing with a sextet component from atomically dispersed Fe-N_x sites contributing with quadrupole doublets.[30] The spectra of selected catalysts (**Figure 5**c-f) could be well-fitted with appropriate combinations of doublet and sextet components. The main signal in all catalysts is a quadrupole doublet with quadrupole splitting (QS) values of 0.98-1.13 mm s^{-1} and isomer shift (IS) value of 0.46-0.47 mm s^{-1}, which is assigned to a high-spin O-Fe(III)N_4C_{12} configuration (D1), with O representing an oxygenated species adsorbed on the metal center (**Table 3**).[27,30,79] A second quadrupole doublet with a high IS and high QS is identified, labeled as D3. On the basis of its distinct IS values (0.97-1.20 mm s^{-1}), this component can be unambiguously assigned

to high-spin ferrous centers. While the existence of high spin Fe(II)-N_x sites cannot be excluded, the recent observation that the presence of this D3 component in Fe-N-C materials coincides with the use of Fe-chloride salts for their synthesis suggests that D3 is due to the presence of ferrous-chloride, with the quadrupole doublet signal of $FeCl_2 \cdot 4H_2O$ having Mössbauer parameters (IS and QS values) matching those of D3.[21] As the present series of catalysts is prepared with $FeCl_3$, we assign D3 in the present work to $FeCl_2 \cdot 4H_2O$.[21] Independent experimental evidence for the presence of $FeCl_2$ after $FeCl_3$ chemical vapor deposition on Zn-N-C also supported the assignment of D3.[21] The relative contribution of D3 to the absorption signal in the present work is however small, 5-8% in $FeCl_3$-R/M=2/0.5 and $FeCl_3$-R/M=2/1, and is not observed in $FeCl_3$-R/M=2/2 or $FeCl_3$-R/M=2/2.5. For the latter two, another quadrupole doublet with IS comparable to D1 but with higher QS (2.85 mm s^{-1}) is observed, labeled D2, accounting for around 20% of the signal. This doublet is commonly co-observed with the D1 component in Mössbauer spectra of Fe-N-C catalysts and assigned to a low or medium spin Fe(II)N_4 configuration.[79] The ferrous state of D2 may be explained by its location in the bulk of the carbon matrix, or by a low affinity with O_2. The presence of D2 in the catalyst prepared with the highest melamine content coincides with a decreasing BET area (**Table 1**), supporting that the minor D2 contribution may result from the non-accessibility of O_2 to some Fe-N_x sites. Mössbauer spectroscopy identifies in addition an important contribution from a broad sextet in $FeCl_3$-R/M=2/0.5, which is assigned to high-spin ferric oxide.[59] The high linewidth (3.19 mm s^{-1}, **Table 3**) supports ultra-small clusters, that are not fully magnetically ordered at -268 ºC. No sextet is detected in the spectra of $FeCl_3$-R/M=2/1 and $FeCl_3$-R/M=2/2, while two well-defined sextets (LW of only 0.27 mm s^{-1}) are identified in the spectrum of $FeCl_3$-R/M=2/2.5, assigned to ferric oxides, but accounting for only 8% of the signal (**Table 3**). Therefore, Mössbauer spectroscopy confirms the XANES and EXAFS results, but also provides more quantitative insights, especially identifying an important contribution from ultra-small iron oxide clusters for samples prepared at low R/M value. This shows that the addition of melamine is crucial for the formation of Fe-N_x sites during the first pyrolysis. Without melamine or with too little melamine, iron probably mainly forms metallic or metal carbide species during pyrolysis. Upon exposure to air or acid washing, these particles can remain in zerovalent state if they are perfectly covered by a graphite shell, or they can be converted partially or fully to iron oxides, depending on oxygen/proton accessibility to the surface of these particles and depending on the particle size. The iron oxide signal in $FeCl_3$-R/M=2/0.5 must thus be a consequence of the presence of iron zerovalent particles after the first pyrolysis stage. Fe cations in an acid solution can indeed partially reprecipitate, depending on the acid nature, temperature, and local iron concentration. Together with the ICP-MS data, we can conclude that nitrogen introduced by M can bind the iron atoms and stabilize them to avoid the formation of iron nanoparticles, with optimized

M content. Last but not least, the signal/noise ratio and absolute signal intensity of the Mössbauer absorption spectra also reflect the Fe content in the samples, with low signal and high noise for the sample with low melamine content (R/M=2/0.5). The major contribution of D1 in this series of catalysts (increasing absolute absorption intensity of D1 with the melamine content) also suggests that the nitrogen species involved in coordinating iron in D1 sites is pyrrolic nitrogen. Pyrrolic nitrogen was indeed shown by XPS to be absent in the sample prepared with R/M=2/0 and to continuously increase with increasing M content. Moreover, the presence of D2 site at high M content can explain decreased pyrrolic N/Fe value because Fe atoms in D2 site are coordinated by pyridinic N. We then corrected the Fe content by percentage of D1 in **Table 3**. In this case, the values of $FeCl_3$-R/M=2/2 and $FeCl_3$-R/M=2/2.5 in **Table 2** become 4.2 and 4.0, respectively, which correspond well to the stoichiometry in Fe-N_4 sites.

Table 3. Spectral parameters derived from the fitting of Mössbauer spectra. Isomer shift (IS), quadrupole splitting (QS), Linewidth (LW), Hyperfine Field (H) and relative signal area (%).

R/M	component	IS / mm s^{-1}	QS / mm s^{-1}	LW / mm s^{-1}	H / T	Relative area %
2/0.5	D1	0.47	0.98	1.26	-	54
	D3	1.20	2.72	0.50	-	5
	Sextet 1	1.19	-	3.19	43	41
2/1	D1	0.47	1.10	1.25	-	92
	D3	0.97	2.90	0.69	-	8
2/2	D1	0.32	1.07	0.89	-	76
	D2	0.56	2.62	1.44	-	24
2/2.5	D1	0.46	1.13	1.04	-	76
	D2	0.45	2.85	2.41	-	16
	Sextet 1	0.69	-0.1	0.27	43.5	3
	Sextet 2	0.65	+0.1	0.27	53.7	5

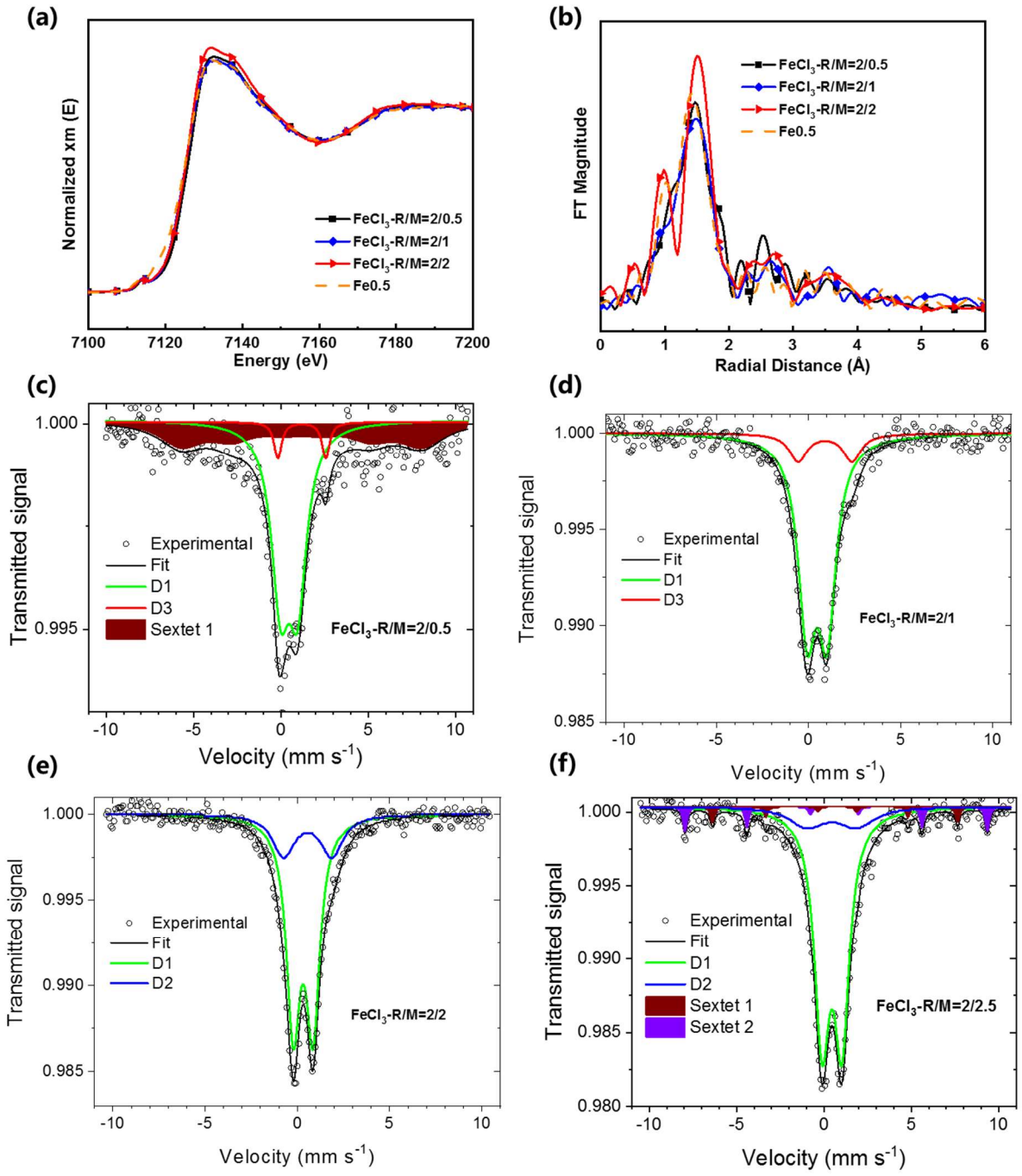

Figure 5. (a) XANES and (b) Fourier transforms of the EXAFS spectra measured at Fe K-edge. Mössbauer spectroscopy characterization of selected catalysts. (c) $FeCl_3$-R/M = 2/0.5, (d) $FeCl_3$-R/M = 2/1, (e) $FeCl_3$-R/M = 2/2, and (f) $FeCl_3$-R/M = 2/2.5. The spectra were acquired at -268°C.

Electrochemical characterization

The polarization curves of catalysts show increasing half-wave potential with increasing M content up to R/M = 2/2, while at R/M = 2/2.5, the activity seems to reach a plateau or even decrease slightly

(**Figure 6**a). All polarization curves except those of $FeCl_3$-R/M=2/0 and $FeCl_3$-R/M=2/2.5 present a sharp kinetic-to-diffusion transition region, indicative of adequate mass-transport properties, at least in RDE setup.[59] The polarization curves were corrected from O_2 diffusion in solution, pseudocapacitive current, and Ohmic resistance to draw Tafel plots (**Figure 6**b). The catalysts exhibit similar Tafel slopes around 60 mV dec^{-1}, which is consistent with the literature and demonstrates that the rate-determining step of the ORR mechanism is the same in this series of catalysts.[18,36,80,81] This is in line with the dominant signal from the component D1 in the Mössbauer spectra, supporting that the change in ORR activity is mainly due to a change in the number of sites, while the fundamental ORR mechanism on the active sites is unmodified. The polarization curves were also used to determine the mass activity of the catalysts at 0.8 V *vs*. RHE ($MA_{0.8}$) after normalization by the catalyst loading (0.4 mg cm^{-2}), as listed in **Table S3**. The mass activity increases *ca.* 4-fold from R/M = 2/0 to 2/1 (0.47 to 2.04 A g^{-1}), then increases slowly from 2/1 to 2/2 (2.04 to 3.00 A g^{-1}) and decreases slightly at R/M = 2/2.5 (2.22 A g^{-1}). The mass activity for the optimized material, $FeCl_3$-R/M=2/2, is only slightly lower than that of the commercial Fe-N-C catalyst (Pajarito powder PMF D14401, 4.04 A g^{-1} as seen in **Figure 6**a). In the search for structure-property relationships, **Figure 6**c plots the mass activity of catalysts as a function of their Fe content obtained from ICP-MS. A linear trend can be observed up to the Fe content of 0.3 at.% (1.36 wt.%), corresponding to the catalyst $FeCl_3$-R/M=2/2, with the highest mass activity 3.0 A g^{-1} for this series. This trend is explained by Mössbauer spectroscopy, showing that most of Fe are present as atomically dispersed Fe-N_x sites, except at low melamine content. Thus, as the bulk Fe content increases, the site density also expectedly increases. Further increasing the M content (and the Fe content) results in a slight decline of the activity due to the restricted mass transfer. The very low mesopore volume in $FeCl_3$-R/M=2/2.5 prevents reactants in the electrolyte from accessing the active sites. This can be demonstrated by its higher Tafel slope (79 mV dec^{-1}), representing a slow kinetic-to-diffusion transition region.[59] The mass activity also shows a positive correlation with the pyrrolic N content obtained from XPS analysis (**Figure 6**d), which further demonstrates the Fe-N_4 active sites are constructed by pyrrolic N. Interestingly, the activity of our catalysts shows little relationship with micropore volume, which is generally considered as an indicator of the number of active sites.[16,18,30,77] This lack of correlation is due to the limitation of active Fe at low M content, not by micropores, in the present synthetic approach.

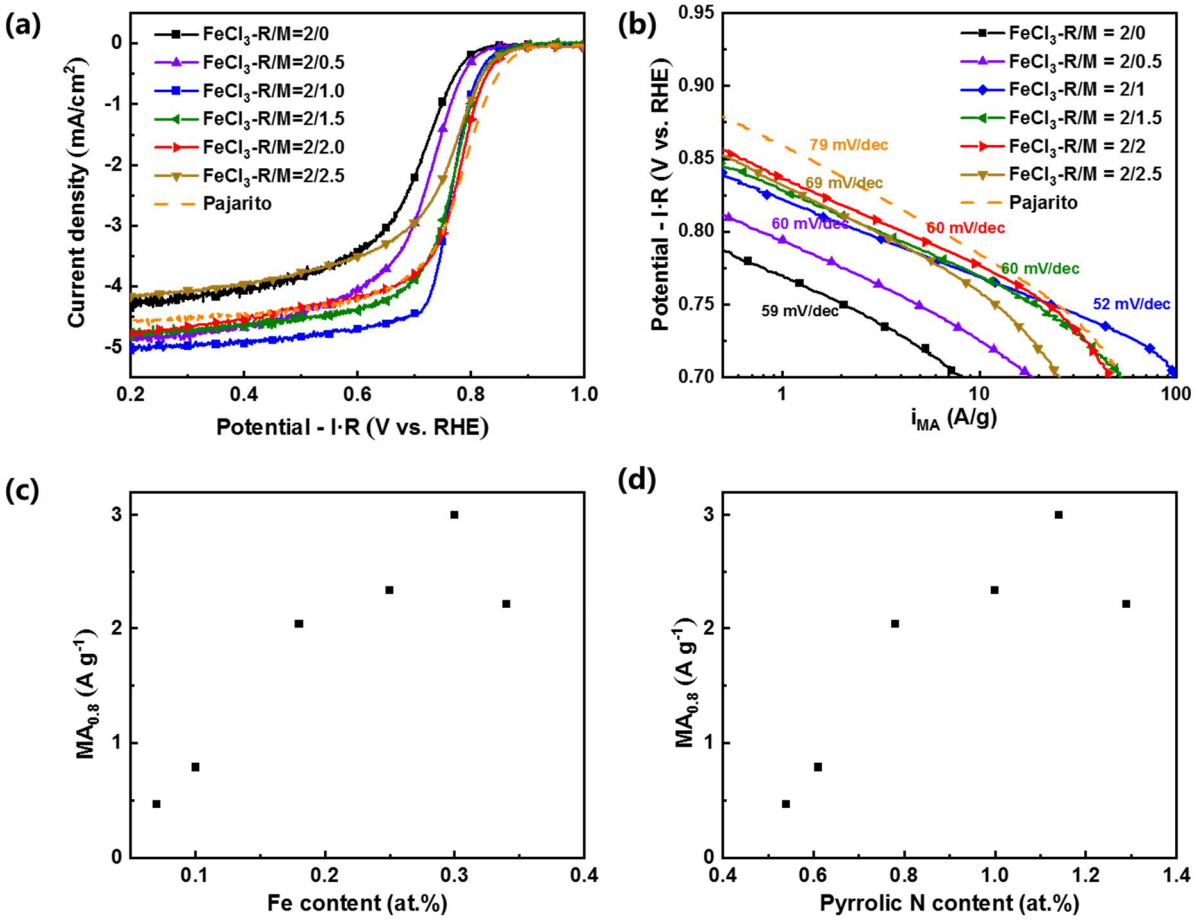

Figure 6. Electrochemical characterization of catalysts prepared from different R/M ratios recorded in 0.05 M H_2SO_4. (a) Polarization curves in O_2-saturated electrolyte at ω = 1600 rpm and v = 10 mV s^{-1}; (b) Tafel plots of the O_2-transport and background-current corrected kinetic current obtained from the steady-state Ohmic drop-corrected *I–E* curves at ω= 1600 rpm; relationships between (c) mass activity in RDE setup and Fe content, (d) mass activity in RDE setup and pyrrolic N content.

To gain further insights into the fundamental reasons for the evolution of the mass activity with the melamine content, the SD and the TOF (**Table S3** and **Figure S4-S9**) were evaluated using the nitrite adsorption/reduction electrochemical method.[34] The SD value increases with M content from R/M=2/0 to 2/1, reaching the maximum value of 8.04×10^{18} sites g^{-1}, whereas it then declines when further increasing M content. These results are not in agreement with our previous conclusion that the increasing mass activity is because the increasing Fe content leads to higher SD values, instead of TOF. To explain this discrepancy, note that the decline of SD when M content increased from R/M=2/1 to 2/1.5 coincides with a sharp decrease of the mesopore volume, which may limit the accessibility of reductive NO_2^- to active sites.[34] Therefore, the SD values at high M content may be

underestimated. This agrees with the research of Strasser et al. that some Fe surface sites located deep inside micropores are inaccessible to NO_2^-. The SD measured by nitrite stripping can thus be regarded as the low bound of Fe-N-C catalysts.[82] On the contrary, the SD value measured at low M content is likely overestimated, because the increase of SD value from R/M = 2/0 to 2/1 is much lower than the increase in mass activity from R/M = 2/0 to 2/1 (*ca.*2 folds of SD *vs. ca.* 4 folds of mass activity). The unexpected high SD measured at low R/M can be explained by the lack of selectivity of the nitrite stripping method, which counts not only Fe-N_x sites on the surface but also Fe oxides. This caveat of the nitrite stripping method had been unveiled in the frame of a study on the degradation mechanisms of Fe-N-C in O_2 saturated acidic solution.[83] The significant presence of Fe oxides is detected by ^{57}Fe Mössbauer spectroscopy in $FeCl_3$-R/M=2/0.5 (accounting for 41 % of the signal intensity), and it can be hypothesized that even more Fe oxides would be present in $FeCl_3$-R/M=2/0. Combining the two factors, the variation of SD with M content becomes moderate and seems uncorrelated with mass activity. In summary, the results of nitrite stripping must be analyzed with caution according to the characteristics of the catalyst.

The ORR activity and power performance of these catalysts were then investigated in a 5 cm^2 single cell PEMFC. Prior to screening all the catalysts, the Nafion/Catalyst (N/C) ratio in the cathode ink formulation was first optimized with $FeCl_3$-R/M=2/1. The high S_{BET} of all catalysts in this study, and high mesopore volume for some of the catalysts, may require more Nafion in the cathode active layer than Pt/C catalysts (*e.g.* Pt on Vulcan, with Vulcan XC72 having S_{BET} of 200-250 m^2 g^{-1} or TEC10E20E, *ca* 800 m^2 g^{-1}). **Figure S10**a shows the effect of the Nafion content in the cathode ink formulation, with both the activity and power performance dramatically increasing from N/C = 1 to N/C = 2, and thereafter only slightly decreasing from N/C = 2 to 2.5. Nyquist plots of electrochemical impedance spectroscopy showed little change with N/C (**Figure S10**b), while cathode CVs recorded in H_2/N_2 PEMFC mode showed dramatically increasing capacitive currents from N/C = 1 to N/C = 2 and only very slightly increasing from N/C = 2 to 2.5 (**Figure S10**c). Therefore, the data indicate that the optimum N/C ratio is 2 for this catalyst, necessary for covering most of the catalyst surface with ionomer (maximizing the activity) without leading to excessive ionomer thickness (minimizing O_2 diffusion issues through the film, and the filling of meso-macropores). This optimum N/C ratio for the Fe-N-C aerogel catalyst in PEMFC is comparable to the one optimized for two other high S_{BET} Fe-N-C catalysts (with a similar PEMFC cathode preparation method).[84] For the two catalysts labeled as ball milling Fe-N-C catalysts 1 and 2 in that work, the optimum N/C ratio was found to be 1.75 and 2, respectively, while their S_{BET} values were 730 and 1000 m^2 g^{-1}, respectively. The S_{BET} values of the series of catalysts in the present work are *ca*. 1100-1600 m^2 g^{-1} and the optimum ratio N/C of

2 is therefore in line with previous results. The other catalysts were then investigated with a fixed N/C value of 2. **Figure 7**a shows the H_2/O_2 polarization curves of all catalysts, with trends in activity at 0.8 V and overall cell performance in line with the trends observed in RDE. For a quantitative comparison of ORR activity trend with the melamine content, **Figure 7**b reports the current density at 0.8 V in PEMFC (a voltage at which the current density is mostly controlled by ORR kinetics) as a function of the melamine content during aerogel preparation. It can be seen that the trend and proportional change of activity with M are similar to that observed in RDE (**Figure 6**c), increasing by a factor of 4 from R/M = 2/0 to 2/2, and thereafter decreasing by about 35% from R/M = 2/2 to 2/2.5. The highest current density at 0.8 V cell voltage is achieved to 104 mA cm^{-2} at R/M=2/2 and the maximum power density (P_{max}) is 0.549 W cm^{-2}. Similar observed activity trends in RDE and PEMFC support that the N/C ratio of 2 for the PEMFC cathode is appropriate for all catalysts of the present series, otherwise lower-than-expected activity would have been observed for some materials in PEMFC. The cell performance of commercial Fe-N-C catalyst (Pajarito Powder, PMF D14401) was also tested under the same condition (**Figure S11**a). While the commercial catalyst showed slightly higher ORR activity in RDE setup than that of the most active catalyst ($FeCl_3$-R/M=2/2 in **Figure 6**b), its current density at 0.8 V in PEMFC is lower than that of any of the aerogel derived catalysts. This indicates unoptimized cathode preparation for the commercial catalyst. The high hydrophobicity of Fe-N-C catalysts derived from silica-templating (as is the case for this commercial catalyst) may require a totally different ink formulation than for hydrophilic Fe-N-C catalysts. The PEMFC data obtained herein on the commercial catalyst can therefore not be used for comparison with the performance of the aerogel-derived catalysts. As an alternative, Tatyana *et al.* recently reported a high-performance mesopore textured Fe-N-C catalyst (Pajarito Powder 230-002-C29) with P_{max} = 0.645 W cm^{-2} in H_2-O_2 PEMFC, which is only slightly higher than our best catalyst.[22] H_2/air PEMFC polarization curves are shown in **Figure 7**c, resulting in similar overall trends with R/M as observed with pure O_2, except that the cathode based on the catalyst with the highest melamine content ($FeCl_3$-R/M=2/2.5) seems to suffer from increased mass-transport issues at high current density. This could be related to the quasi-absence of mesopores in this catalyst (0.02 cm^3 g^{-1}, **Table 1**) while $FeCl_3$-R/M=2/2, prepared with less melamine, still shows some mesopores (0.25 cm^3 g^{-1}, **Table 1**). For assessing the oxygen-transport properties of the different Fe-N-C cathodes (different R/M values for aerogel preparation), we compare the current densities measured at 0.3 V (voltage at which mass-transport plays a key role on the current density achieved) with pure O_2 or with air (**Figure 7**d). The figure shows that the magnitude of the decrease in current density when switching from O_2 to air is comparable for all catalysts, despite huge differences in the mesopore volume of this set of catalysts (**Table 1**). One can therefore conclude that mesopores are not a necessary criterion to

reach high PEMFC performance of Fe-N-C catalysts. For the present synthesis approach, the addition of melamine is therefore critical to increase the Fe content, SD, and ORR activity, while it impacts little the mass-transport properties of the cathode active layers. Macropores must exist in the cathode active layers for O_2 and water transport, but cannot be captured by N_2 sorption isotherms measured on the Fe-N-C powders nor cathode layers, the technique having an upper limit of detection of pores with size of *ca.* 100 nm.

In summary, Fe-N-C catalysts with adjustable and high purity Fe-N_4 active sites embedded in a carbon aerogel substrate were synthesized for the first time in this work. The key conclusion regarding the preparation is that an abundant N source is necessary in the aerogel precursor, in order to minimize the yield of Fe-rich nanoparticles. However, it is not a sufficient condition to obtain mainly or only Fe-N_4 active sites. The content of Fe-rich species (especially Fe oxides) cannot be ignored in most Fe-N-C aerogel catalysts derived from the pyrolysis of polymer, even though an acid washing was conducted after the carbonization.[48,85] In our previous work, 47% of the absorption area in the Mössbauer spectrum of a Fe-N-C prepared with R/M = 2/1 was assigned to Fe oxide, 25% to zerovalent Fe (the remainder, 28%, to D1 sites), whereas the Fe-N-C catalyst prepared with the same R/M ratio in the present work shows only 8% of iron chloride particle (D3 signal) and the remainder (92%) is assigned to D1 sites.[59] The main differences between the synthesis methods in this and our former work are ammonia treatment and ball-milling conditions. Between them, a stronger ball-milling condition in the present work is considered to be the main reason for the absence of zerovalent Fe or oxide, *i.e*. 15 min with 10 mm diameter ZrO_2 balls plus 60 min with 5 mm diameter ZrO_2 balls at 400 rpm, whereas only 15 min grind with 10 mm diameter ZrO_2 balls at 400 rpm was applied previously.[58,59] The strong ball-milling condition leads to fin powder size and exposes most of Fe nanoparticles embedded in the pores of carbon aerogel so that they can be eliminated during the acid wash. On the contrary, the Fe-rich nanoparticles embedded in the carbon particles cannot be completely removed by acid washing, as they were detected by Mössbauer spectrum.[59] Due to the advantages of high purity Fe-N_4 active sites and carbon aerogel substrate, Fe-N-C aerogel catalyst with R/M=2/2 exhibits outperformance both in mass activity and mass transport properties, which makes it a promising candidate for application.

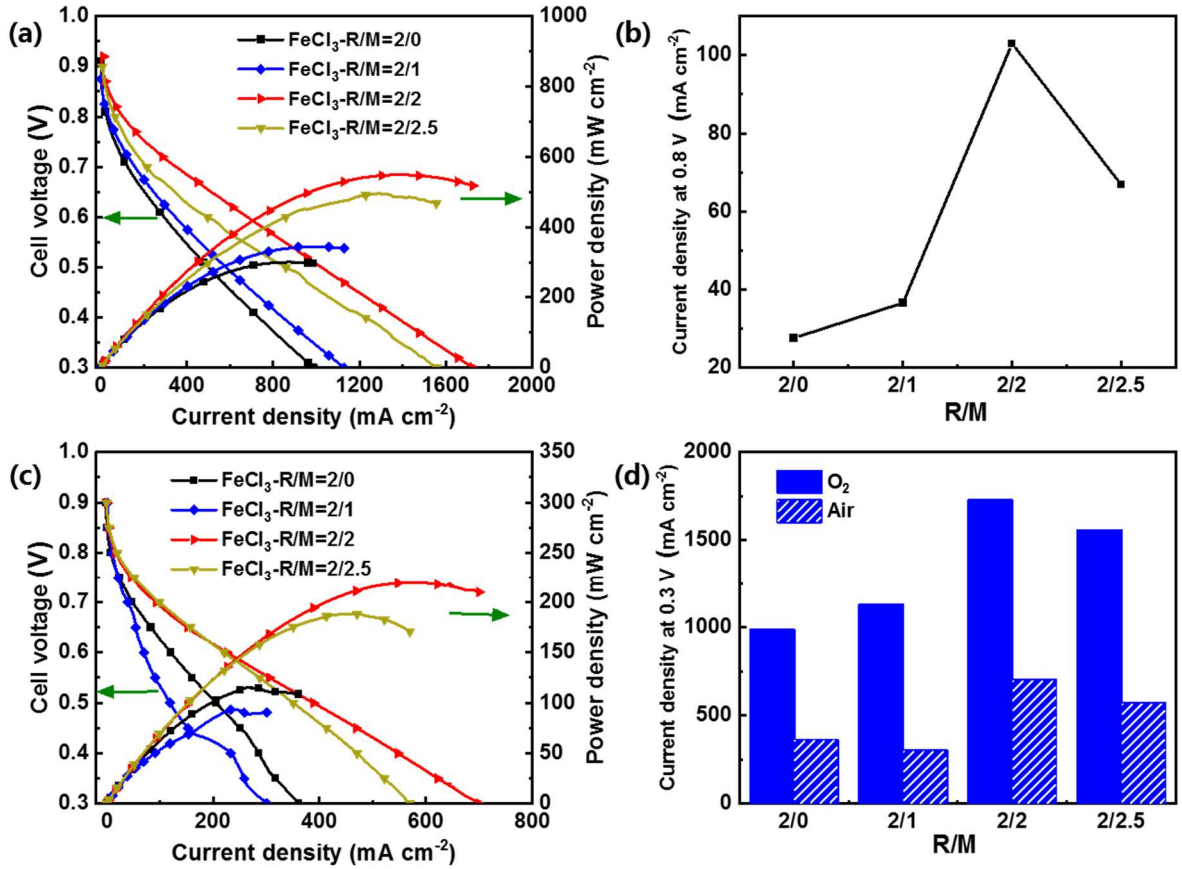

Figure 7. Investigation of the set of aerogel Fe-N-C catalysts as PEMFC cathodes. (a) H_2-O_2 PEMFC polarization and power density curves. (b) Current density at 0.8 V as a function of the melamine content at the aerogel preparation stage. (c) H_2-air PEMFC polarization and power density curves. (d) Comparison of the current density at 0.3 V measured with O_2 or air, for each catalyst. The measurements were performed with T_{cell} = 80°C, 100 % RH, $P_{cathode}$ = P_{anode} = 2 bar_{abs}, and the H_2 and O_2 flow rates were 150 mL min^{-1} while the air flow rate was 480 mL min^{-1}.

Conclusions

In this study, we showed that high melamine content is crucial to obtain only atomically dispersed Fe-N_4 active sites in Fe-N-C aerogel catalysts. The absolute amount of Fe was found to increase with M content, and the absolute amount of Fe-N_4 sites also increases with M content. From the analysis of XPS spectra, the pyrrolic N content is positively correlated with the increase of the M content, supporting that most of the active Fe atoms are coordinated by pyrrolic nitrogen, in agreement with Mössbauer spectra. The atomically mixed nitrogen and Fe in aerogel precursor can stabilize the Fe during pyrolysis, avoiding or minimizing the formation of iron nanoparticles. Electrochemical tests

in RDE show a linear relationship between mass activity up to a Fe content of 0.3 at.%, corresponding to the catalyst $FeCl_3$-R/M=2/2, with the highest mass activity of 3.0 A g^{-1} at 0.8 V vs. RHE. This trend is in line with the physicochemical characterization indicating that most Fe is present as atomically dispersed Fe-N_x sites. Further increase in melamine content (R/M=2/2.5) reduces the mass activity possibly because of the formation of less active D2 sites and low accessibility to the active sites led by a sharp decrease of mesopore. Their ORR performance exhibits a similar trend in PEMFC. No diffusion-limited current density effect is seen in all H_2-air PEMFC polarization curves, indicating excellent mass transport properties of aerogel-based catalysts. Considering the low mesopore volume of the catalyst with high melamine content, the accessibility to the active sites is obtained by the presence of macropores in the cathode active layers.

Supporting information

Details for preparing Fe-N-C aerogel catalysts with different R/M values; assignment of FT-IR spectra; MA toward the ORR, SD, and TOF values in RDE setup; SEM and TEM images; Raman spectra and XRD patterns; deconvolution method of N_{1s} XPS spectrum; CVs and ORR polarization curves of nitrite stripping method to determine SD and TOF values; CVs, ORR polarization curves and Nyquist plots for aerogel catalysts with different ink formulations in PEMFC; ORR polarization curves and Nyquist plots of Pajarito powders with the same ink formulation of aerogel catalyst.

Acknowledgements

The authors thanks Frédéric Georgi (MINES Paris/CEMEF) for XPS analysis. This work was supported by the French National Research Agency in the frame of the ANIMA project (grant number n°ANR-19-CE05-0039) and Coordenação de Aperfeiçoamento de Pessoal de Nível Superior (CAPES) Brazil (grant number 88887.598551/2021-00).

CRediT authorship contribution statement

Hongxin Ge: Writing - original draft, Drawing, Samples synthesis and characterization, Investigation, Formal analysis, Data curation. **Nicolas Bibent:** Investigation, Formal analysis, **Keyla Teixeira Santos**: Sample collection and analysis; Investigation; Formal analysis; Drawing; Data curation. **Kavita Kumar**: Sample collection and analysis; Investigation; Formal analysis; Drawing, Data curation; Writing – review & editing, **Julien Jaxel**: Supercritical drying and SEM analysis, **Moulay Sougrati**: Investigation, Formal analysis, **Andrea Zitolo**: Formal analysis, **Marc Dupont:**

Methodology, **Frédéric Lecoeur:** Methodology, **Vincent Martin**: Methodology; ICP-MS measurements; Formal analysis; Data curation. **Michel Mermoux**: Raman spectroscopy measurements; Formal analysis; Data curation. **Laetitia Dubau**: TEM measurements; Formal analysis; Data curation. **Frédéric Jaouen:** Conceptualization, Writing – review & editing, **Frédéric Maillard**: Conceptualization; Data curation; Funding acquisition; Project administration; Supervision; Validation; Writing – review & editing. **Sandrine Berthon-Fabry**: Conceptualization, Project administration, Formal analysis, Data curation Writing – review & editing.

References

(1) Nazir, H.; Louis, C.; Jose, S.; Prakash, J.; Muthuswamy, N.; Buan, M. E. M.; Flox, C.; Chavan, S.; Shi, X.; Kauranen, P.; Kallio, T.; Maia, G.; Tammeveski, K.; Lymperopoulos, N.; Carcadea, E.; Veziroglu, E.; Iranzo, A.; Kannan, A. M. Is the H2 Economy Realizable in the Foreseeable Future? Part I: H2 Production Methods. *International Journal of Hydrogen Energy* **2020**, *45*, 13777–13788.

(2) Nazir, H.; Muthuswamy, N.; Louis, C.; Jose, S.; Prakash, J.; Buan, M. E.; Flox, C.; Chavan, S.; Shi, X.; Kauranen, P.; Kallio, T.; Maia, G.; Tammeveski, K.; Lymperopoulos, N.; Carcadea, E.; Veziroglu, E.; Iranzo, A.; Kannan, A. M. Is the H2 Economy Realizable in the Foreseeable Future? Part II: H2 Storage, Transportation, and Distribution. *International Journal of Hydrogen Energy* **2020**, *45*, 20693–20708.

(3) Nazir, H.; Muthuswamy, N.; Louis, C.; Jose, S.; Prakash, J.; Buan, M. E. M.; Flox, C.; Chavan, S.; Shi, X.; Kauranen, P.; Kallio, T.; Maia, G.; Tammeveski, K.; Lymperopoulos, N.; Carcadea, E.; Veziroglu, E.; Iranzo, A.; M. Kannan, A. Is the H2 Economy Realizable in the Foreseeable Future? Part III: H2 Usage Technologies, Applications, and Challenges and Opportunities. *International Journal of Hydrogen Energy* **2020**, *45*, 28217–28239.

(4) Zhang, X.; Truong-Phuoc, L.; Asset, T.; Pronkin, S.; Pham-Huu, C. Are Fe–N–C Electrocatalysts an Alternative to Pt-Based Electrocatalysts for the Next Generation of Proton Exchange Membrane Fuel Cells? *ACS Catal.* **2022**, *12*, 13853–13875.

(5) Liang, Y.; Li, Y.; Wang, H.; Zhou, J.; Wang, J.; Regier, T.; Dai, H. Co3O4 Nanocrystals on Graphene as a Synergistic Catalyst for Oxygen Reduction Reaction. *Nature Mater* **2011**, *10*, 780–786.

(6) Kumar, K.; Canaff, C.; Rousseau, J.; Arrii-Clacens, S.; Napporn, T. W.; Habrioux, A.; Kokoh, K. B. Effect of the Oxide–Carbon Heterointerface on the Activity of Co_3O_4/NRGO Nanocomposites toward ORR and OER. *J. Phys. Chem. C* **2016**, *120*, 7949–7958.

(7) Shao, M.; Chang, Q.; Dodelet, J.-P.; Chenitz, R. Recent Advances in Electrocatalysts for Oxygen Reduction Reaction. *Chem. Rev.* **2016**, *116*, 3594–3657.

(8) Zhao, D.; Zhang, S.; Yin, G.; Du, C.; Wang, Z.; Wei, J. Effect of Se in Co-Based Selenides towards Oxygen Reduction Electrocatalytic Activity. *Journal of Power Sources* **2012**, *206*, 103–107.

(9) Gao, M.-R.; Xu, Y.-F.; Jiang, J.; Yu, S.-H. Nanostructured Metal Chalcogenides: Synthesis, Modification, and Applications in Energy Conversion and Storage Devices. *Chem. Soc. Rev.* **2013**, *42*, 2986.

(10) Zhao, D.; Zhang, S.; Yin, G.; Du, C.; Wang, Z.; Wei, J. Tungsten Doped Co–Se Nanocomposites as an Efficient Non Precious Metal Catalyst for Oxygen Reduction. *Electrochimica Acta* **2013**, *91*, 179–184.

(11) Flyagina, I. S.; Hughes, K. J.; Mielczarek, D. C.; Ingham, D. B.; Pourkashanian, M. Identifying the Catalytic Active Sites in Heteroatom-Doped Graphene for the Oxygen Reduction Reaction. *Fuel Cells* **2016**, *16*, 568–576.
(12) Nagy, B.; Villar-Rodil, S.; Tascón, J. M. D.; Bakos, I.; László, K. Nitrogen Doped Mesoporous Carbon Aerogels and Implications for Electrocatalytic Oxygen Reduction Reactions. *Microporous and Mesoporous Materials* **2016**, *230*, 135–144.
(13) Tan, H.; Tang, J.; Kim, J.; Kaneti, Y. V.; Kang, Y.-M.; Sugahara, Y.; Yamauchi, Y. Rational Design and Construction of Nanoporous Iron- and Nitrogen-Doped Carbon Electrocatalysts for Oxygen Reduction Reaction. *J. Mater. Chem. A* **2019**, *7*, 1380–1393.
(14) Jaouen, F.; Marcotte, S.; Dodelet, J.-P.; Lindbergh, G. Oxygen Reduction Catalysts for Polymer Electrolyte Fuel Cells from the Pyrolysis of Iron Acetate Adsorbed on Various Carbon Supports. *J. Phys. Chem. B* **2003**, *107*, 1376–1386.
(15) Lefèvre, M.; Proietti, E.; Jaouen, F.; Dodelet, J.-P. Iron-Based Catalysts with Improved Oxygen Reduction Activity in Polymer Electrolyte Fuel Cells. *Science* **2009**, *324*, 71–74.
(16) Yang, Z.; Wang, Y.; Zhu, M.; Li, Z.; Chen, W.; Wei, W.; Yuan, T.; Qu, Y.; Xu, Q.; Zhao, C.; Wang, X.; Li, P.; Li, Y.; Wu, Y.; Li, Y. Boosting Oxygen Reduction Catalysis with Fe–N_4 Sites Decorated Porous Carbons toward Fuel Cells. *ACS Catal.* **2019**, *9*, 2158–2163.
(17) Santori, P. G.; Speck, F. D.; Li, J.; Zitolo, A.; Jia, Q.; Mukerjee, S.; Cherevko, S.; Jaouen, F. Effect of Pyrolysis Atmosphere and Electrolyte PH on the Oxygen Reduction Activity, Stability and Spectroscopic Signature of FeN_x Moieties in Fe-N-C Catalysts. *J. Electrochem. Soc.* **2019**, *166*, F3311–F3320.
(18) Xiao, M.; Zhu, J.; Ma, L.; Jin, Z.; Ge, J.; Deng, X.; Hou, Y.; He, Q.; Li, J.; Jia, Q.; Mukerjee, S.; Yang, R.; Jiang, Z.; Su, D.; Liu, C.; Xing, W. Microporous Framework Induced Synthesis of Single-Atom Dispersed Fe-N-C Acidic ORR Catalyst and Its in Situ Reduced Fe-N_4 Active Site Identification Revealed by X-Ray Absorption Spectroscopy. *ACS Catal.* **2018**, *8*, 2824–2832.
(19) Liu, S.; Li, C.; Zachman, M. J.; Zeng, Y.; Yu, H.; Li, B.; Wang, M.; Braaten, J.; Liu, J.; Meyer, H. M.; Lucero, M.; Kropf, A. J.; Alp, E. E.; Gong, Q.; Shi, Q.; Feng, Z.; Xu, H.; Wang, G.; Myers, D. J.; Xie, J.; Cullen, D. A.; Litster, S.; Wu, G. Atomically Dispersed Iron Sites with a Nitrogen–Carbon Coating as Highly Active and Durable Oxygen Reduction Catalysts for Fuel Cells. *Nat Energy* **2022**, *7*, 652–663.
(20) Mehmood, A.; Gong, M.; Jaouen, F.; Roy, A.; Zitolo, A.; Khan, A.; Sougrati, M.-T.; Primbs, M.; Bonastre, A. M.; Fongalland, D.; Drazic, G.; Strasser, P.; Kucernak, A. High Loading of Single Atomic Iron Sites in Fe–NC Oxygen Reduction Catalysts for Proton Exchange Membrane Fuel Cells. *Nat Catal* **2022**, *5*, 311–323.
(21) Jiao, L.; Li, J.; Richard, L. L.; Sun, Q.; Stracensky, T.; Liu, E.; Sougrati, M. T.; Zhao, Z.; Yang, F.; Zhong, S.; Xu, H.; Mukerjee, S.; Huang, Y.; Cullen, D. A.; Park, J. H.; Ferrandon, M.; Myers, D. J.; Jaouen, F.; Jia, Q. Chemical Vapour Deposition of Fe–N–C Oxygen Reduction Catalysts with Full Utilization of Dense Fe–N4 Sites. *Nat. Mater.* **2021**, *20*, 1385–1391.
(22) Akula, S.; Mooste, M.; Zulevi, B.; McKinney, S.; Kikas, A.; Piirsoo, H.-M.; Rähn, M.; Tamm, A.; Kisand, V.; Serov, A.; Creel, E. B.; Cullen, D. A.; Neyerlin, K. C.; Wang, H.; Odgaard, M.; Reshetenko, T.; Tammeveski, K. Mesoporous Textured Fe-N-C Electrocatalysts as Highly Efficient Cathodes for Proton Exchange Membrane Fuel Cells. *Journal of Power Sources* **2022**, *520*, 230819.
(23) Kisand, K.; Sarapuu, A.; Douglin, J. C.; Kikas, A.; Treshchalov, A.; Käärik, M.; Piirsoo, H.-M.; Paiste, P.; Aruväli, J.; Leis, J.; Kisand, V.; Tamm, A.; Dekel, D. R.; Tammeveski, K. Templated Nitrogen-, Iron-, and Cobalt-Doped Mesoporous Nanocarbon Derived from an Alkylresorcinol Mixture for Anion-Exchange Membrane Fuel Cell Application. *ACS Catal.* **2022**, *12*, 14050–14061.

(24) Ohms, D.; Herzog, S.; Franke, R.; Neumann, V.; Wiesener, K.; Gamburcev, S.; Kaisheva, A.; Iliev, I. Influence of Metal Ions on the Electrocatalytic Oxygen Reduction of Carbon Materials Prepared from Pyrolyzed Polyacrylonitrile. *Journal of Power Sources* **1992**, *38*, 327–334.
(25) Herrmann, I.; Kramm, U. I.; Radnik, J.; Fiechter, S.; Bogdanoff, P. Influence of Sulfur on the Pyrolysis of CoTMPP as Electrocatalyst for the Oxygen Reduction Reaction. *J. Electrochem. Soc.* **2009**, *156*, B1283.
(26) Wu, G.; Johnston, C. M.; Mack, N. H.; Artyushkova, K.; Ferrandon, M.; Nelson, M.; Lezama-Pacheco, J. S.; Conradson, S. D.; More, K. L.; Myers, D. J.; Zelenay, P. Synthesis–Structure–Performance Correlation for Polyaniline–Me–C Non-Precious Metal Cathode Catalysts for Oxygen Reduction in Fuel Cells. *J. Mater. Chem.* **2011**, *21*, 11392.
(27) Zitolo, A.; Goellner, V.; Armel, V.; Sougrati, M.-T.; Mineva, T.; Stievano, L.; Fonda, E.; Jaouen, F. Identification of Catalytic Sites for Oxygen Reduction in Iron- and Nitrogen-Doped Graphene Materials. *Nature Mater* **2015**, *14*, 937–942.
(28) Zagal, J. H.; Koper, M. T. M. Reactivity Descriptors for the Activity of Molecular MN4 Catalysts for the Oxygen Reduction Reaction. *Angew. Chem. Int. Ed.* **2016**, *55*, 14510–14521.
(29) Marshall-Roth, T.; Libretto, N. J.; Wrobel, A. T.; Anderton, K. J.; Pegis, M. L.; Ricke, N. D.; Voorhis, T. V.; Miller, J. T.; Surendranath, Y. A Pyridinic Fe-N4 Macrocycle Models the Active Sites in Fe/N-Doped Carbon Electrocatalysts. *Nat Commun* **2020**, *11*, 5283.
(30) Li, J.; Sougrati, M. T.; Zitolo, A.; Ablett, J. M.; Oğuz, I. C.; Mineva, T.; Matanovic, I.; Atanassov, P.; Huang, Y.; Zenyuk, I.; Di Cicco, A.; Kumar, K.; Dubau, L.; Maillard, F.; Dražić, G.; Jaouen, F. Identification of Durable and Non-Durable FeNx Sites in Fe–N–C Materials for Proton Exchange Membrane Fuel Cells. *Nat Catal* **2021**, *4*, 10–19.
(31) Li, J.; Jiao, L.; Wegener, E.; Richard, L. L.; Liu, E.; Zitolo, A.; Sougrati, M.-T.; Mukerjee, S.; Zhao, Z.; Huang, Y.; Yang, F.; Zhong, S.; Xu, H.; Kropf, A. J.; Jaouen, F.; Myers, D. J.; Jia, Q. The Evolution Pathway from Iron Compounds to Fe1(II)-N4 Sites through Gas-Phase Iron during Pyrolysis. *Journal of the American Chemical Society* **2020**, *142*, 1412–1423.
(32) Kramm, U. I.; Herranz, J.; Larouche, N.; Arruda, T. M.; Lefèvre, M.; Jaouen, F.; Bogdanoff, P.; Fiechter, S.; Abs-Wurmbach, I.; Mukerjee, S.; Dodelet, J.-P. Structure of the Catalytic Sites in Fe/N/C-Catalysts for O2-Reduction in PEM Fuel Cells. *Phys. Chem. Chem. Phys.* **2012**, *14*, 11673.
(33) Ferrandon, M.; Kropf, A. J.; Myers, D. J.; Artyushkova, K.; Kramm, U.; Bogdanoff, P.; Wu, G.; Johnston, C. M.; Zelenay, P. Multitechnique Characterization of a Polyaniline–Iron–Carbon Oxygen Reduction Catalyst. *J. Phys. Chem. C* **2012**, *116*, 16001–16013.
(34) Kumar, K.; Asset, T.; Li, X.; Liu, Y.; Yan, X.; Chen, Y.; Mermoux, M.; Pan, X.; Atanassov, P.; Maillard, F.; Dubau, L. Fe–N–C Electrocatalysts' Durability: Effects of Single Atoms' Mobility and Clustering. *ACS Catal.* **2021**, *11*, 484–494.
(35) Herranz, J.; Jaouen, F.; Lefèvre, M.; Kramm, U. I.; Proietti, E.; Dodelet, J.-P.; Bogdanoff, P.; Fiechter, S.; Abs-Wurmbach, I.; Bertrand, P.; Arruda, T. M.; Mukerjee, S. Unveiling N-Protonation and Anion-Binding Effects on Fe/N/C Catalysts for O $_2$ Reduction in Proton-Exchange-Membrane Fuel Cells. *J. Phys. Chem. C* **2011**, *115*, 16087–16097.
(36) Sgarbi, R.; Kumar, K.; Jaouen, F.; Zitolo, A.; Ticianelli, E. A.; Maillard, F. Oxygen Reduction Reaction Mechanism and Kinetics on M-NxCy and M@N-C Active Sites Present in Model M-N-C Catalysts under Alkaline and Acidic Conditions. *J Solid State Electrochem* **2021**, *25*, 45–56.
(37) Proietti, E.; Jaouen, F.; Lefèvre, M.; Larouche, N.; Tian, J.; Herranz, J.; Dodelet, J.-P. Iron-Based Cathode Catalyst with Enhanced Power Density in Polymer Electrolyte Membrane Fuel Cells. *Nat Commun* **2011**, *2*, 416.
(38) Chung, H. T.; Cullen, D. A.; Higgins, D.; Sneed, B. T.; Holby, E. F.; More, K. L.; Zelenay, P. Direct Atomic-Level Insight into the Active Sites of a High-Performance PGM-Free ORR Catalyst. *Science* **2017**, *357*, 479–484.

(39) Robson, M. H.; Serov, A.; Artyushkova, K.; Atanassov, P. A Mechanistic Study of 4-Aminoantipyrine and Iron Derived Non-Platinum Group Metal Catalyst on the Oxygen Reduction Reaction. *Electrochimica Acta* **2013**, *90*, 656–665.
(40) Serov, A.; Artyushkova, K.; Atanassov, P. Fe-N-C Oxygen Reduction Fuel Cell Catalyst Derived from Carbendazim: Synthesis, Structure, and Reactivity. *Advanced Energy Materials* **2014**, *4*, 1301735.
(41) Serov, A.; Robson, M. H.; Artyushkova, K.; Atanassov, P. Templated Non-PGM Cathode Catalysts Derived from Iron and Poly(Ethyleneimine) Precursors. *Applied Catalysis B: Environmental* **2012**, *127*, 300–306.
(42) Brocato, S.; Serov, A.; Atanassov, P. PH Dependence of Catalytic Activity for ORR of the Non-PGM Catalyst Derived from Heat-Treated Fe–Phenanthroline. *Electrochimica Acta* **2013**, *87*, 361–365.
(43) ElKhatat, A. M.; Al-Muhtaseb, S. A. Advances in Tailoring Resorcinol-Formaldehyde Organic and Carbon Gels. *Adv. Mater.* **2011**, *23*, 2887–2903.
(44) Horikawa, T.; Hayashi, J.; Muroyama, K. Controllability of Pore Characteristics of Resorcinol–Formaldehyde Carbon Aerogel. *Carbon* **2004**, *42*, 1625–1633.
(45) Zhou, H.; Xu, S.; Su, H.; Wang, M.; Qiao, W.; Ling, L.; Long, D. Facile Preparation and Ultra-Microporous Structure of Melamine–Resorcinol–Formaldehyde Polymeric Microspheres. *Chem. Commun.* **2013**, *49*, 3763.
(46) Al-Muhtaseb, S. A.; Ritter, J. A. Preparation and Properties of Resorcinol-Formaldehyde Organic and Carbon Gels. *Adv. Mater.* **2003**, *15*, 101–114.
(47) Rasines, G.; Lavela, P.; Macías, C.; Zafra, M. C.; Tirado, J. L.; Parra, J. B.; Ania, C. O. N-Doped Monolithic Carbon Aerogel Electrodes with Optimized Features for the Electrosorption of Ions. *Carbon* **2015**, *83*, 262–274.
(48) Kiciński, W.; Dyjak, S.; Tokarz, W. Carbon Gel-Derived Fe–N–C Electrocatalysts for Hydrogen-Air Polymer Electrolyte Fuel Cells. *Journal of Power Sources* **2021**, *513*, 230537.
(49) Roiron, C.; Celle, C.; Jacques, P.-A.; Heitzmann, M.; Simonato, J.-P. Structure–Property Relationship of Cryogel-Based Fe–N–C Catalysts for the Oxygen Reduction Reaction. *Energy Fuels* **2021**, *35*, 16814–16821.
(50) Elumeeva, K.; Ren, J.; Antonietti, M.; Fellinger, T.-P. High Surface Iron/Cobalt-Containing Nitrogen-Doped Carbon Aerogels as Non-Precious Advanced Electrocatalysts for Oxygen Reduction. *ChemElectroChem* **2015**, *2*, 584–591.
(51) Hao, R.; Gu, S.; Chen, J.; Wang, Z.; Gan, Q.; Wang, Z.; Huang, Y.; Liu, P.; Zhang, K.; Liu, K.; Liu, C.; Lu, Z. Microporous Fe–N4 Cataysts Derived from Biomass Aerogel for a High-Performance Zn–Air Battery. *Materials Today Energy* **2021**, *21*, 100826.
(52) Cui, X.; Yang, S.; Yan, X.; Leng, J.; Shuang, S.; Ajayan, P. M.; Zhang, Z. Pyridinic-Nitrogen-Dominated Graphene Aerogels with Fe–N–C Coordination for Highly Efficient Oxygen Reduction Reaction. *Advanced Functional Materials* **2016**, *26*, 5708–5717.
(53) Ma, Y.; Chen, D.; Zhang, D.; Yu, H.; Zheng, Y.; Li, W.; Wang, L.; Liu, Q.; Yang, W. Fe,N-Modulated Carbon Fibers Aerogel as Freestanding Cathode Catalyst for Rechargeable Zn–Air Battery. *Carbon* **2022**, *187*, 196–206.
(54) Wang, H.; Pang, Y.; Mo, Z.; Wang, X.; Ren, J.; Wang, R. Performance Evaluation of Functionalized Carbon Aerogel as Oxygen Reduction Reaction Electrocatalyst in Zinc-Air Cell. *Journal of Power Sources* **2021**, *511*, 230458.
(55) Zion, N.; Cullen, D. A.; Zelenay, P.; Elbaz, L. Heat-Treated Aerogel as a Catalyst for the Oxygen Reduction Reaction. *Angew. Chem. Int. Ed.* **2020**, *59*, 2483–2489.
(56) Zion, N.; Peles-Strahl, L.; Friedman, A.; Cullen, D. A.; Elbaz, L. Electrocatalysis of Oxygen Reduction Reaction in a Polymer Electrolyte Fuel Cell with a Covalent Framework of Iron Phthalocyanine Aerogel. *ACS Appl. Energy Mater.* **2022**, *5*, 7997–8003.

(57) Zion, N.; Douglin, J. C.; Cullen, D. A.; Zelenay, P.; Dekel, D. R.; Elbaz, L. Porphyrin Aerogel Catalysts for Oxygen Reduction Reaction in Anion-Exchange Membrane Fuel Cells. *Adv. Funct. Mater.* **2021**, *31*, 2100963.
(58) Wang, Y.; Berthon-Fabry, S. One-Pot Synthesis of Fe-N-Containing Carbon Aerogel for Oxygen Reduction Reaction. *Electrocatalysis* **2021**, *12*, 78–90.
(59) Wang, Y.; Larsen, M. J.; Rojas, S.; Sougrati, M.-T.; Jaouen, F.; Ferrer, P.; Gianolio, D.; Berthon-Fabry, S. Influence of the Synthesis Parameters on the Proton Exchange Membrane Fuel Cells Performance of Fe–N–C Aerogel Catalysts. *Journal of Power Sources* **2021**, *514*, 230561.
(60) Li, X.; Liu, Y.; Chen, H.; Yang, M.; Yang, D.; Li, H.; Lin, Z. Rechargeable Zn–Air Batteries with Outstanding Cycling Stability Enabled by Ultrafine FeNi Nanoparticles-Encapsulated N-Doped Carbon Nanosheets as a Bifunctional Electrocatalyst. *Nano Lett.* **2021**, *21*, 3098–3105.
(61) Sarapuu, A.; Kreek, K.; Kisand, K.; Kook, M.; Uibu, M.; Koel, M.; Tammeveski, K. Electrocatalysis of Oxygen Reduction by Iron-Containing Nitrogen-Doped Carbon Aerogels in Alkaline Solution. *Electrochimica Acta* **2017**, *230*, 81–88.
(62) Artyushkova, K.; Serov, A.; Rojas-Carbonell, S.; Atanassov, P. Chemistry of Multitudinous Active Sites for Oxygen Reduction Reaction in Transition Metal–Nitrogen–Carbon Electrocatalysts. *J. Phys. Chem. C* **2015**, *119*, 25917–25928.
(63) Artyushkova, K. Misconceptions in Interpretation of Nitrogen Chemistry from X-Ray Photoelectron Spectra. *Journal of Vacuum Science & Technology A* **2020**, *38*, 031002.
(64) Artyushkova, K.; Atanassov, P. X-Ray Photoelectron Spectroscopy for Characterization of Bionanocomposite Functional Materials for Energy-Harvesting Technologies. *ChemPhysChem* **2013**, *14*, 2071–2080.
(65) Castanheira, L.; Silva, W. O.; Lima, F. H. B.; Crisci, A.; Dubau, L.; Maillard, F. Carbon Corrosion in Proton-Exchange Membrane Fuel Cells: Effect of the Carbon Structure, the Degradation Protocol, and the Gas Atmosphere. *ACS Catal.* **2015**, *5*, 2184–2194.
(66) Knight, D. S.; White, W. B. Characterization of Diamond Films by Raman Spectroscopy. *Journal of Materials Research* **1989**, *4*, 385–393.
(67) Malko, D.; Kucernak, A.; Lopes, T. In Situ Electrochemical Quantification of Active Sites in Fe–N/C Non-Precious Metal Catalysts. *Nat Commun* **2016**, *7*, 13285.
(68) Kim, D. H.; Ringe, S.; Kim, H.; Kim, S.; Kim, B.; Bae, G.; Oh, H.-S.; Jaouen, F.; Kim, W.; Kim, H.; Choi, C. H. Selective Electrochemical Reduction of Nitric Oxide to Hydroxylamine by Atomically Dispersed Iron Catalyst. *Nat Commun* **2021**, *12*, 1856.
(69) Liang, C.; Sha, G.; Guo, S. Resorcinol–Formaldehyde Aerogels Prepared by Supercritical Acetone Drying. *Journal of Non-Crystalline Solids* **2000**, *271*, 167–170.
(70) Liu, L.; Deng, Q.-F.; Ma, T.-Y.; Lin, X.-Z.; Hou, X.-X.; Liu, Y.-P.; Yuan, Z.-Y. Ordered Mesoporous Carbons: Citric Acid-Catalyzed Synthesis, Nitrogen Doping and CO2 Capture. *J. Mater. Chem.* **2011**, *21*, 16001.
(71) Higashimoto, S.; Sasakura, Y.; Tokunaga, R.; Takahashi, M.; Kobayashi, H.; Jiang, J.; Sakata, Y. Synthesis, Characterization and Photocatalytic Properties of Robust Resorcinol-Formaldehyde Polymer Fine Particles. *Applied Catalysis A: General* **2021**, *623*, 118240.
(72) Weiss, S.; Urdl, K.; Mayer, H. A.; Zikulnig-Rusch, E. M.; Kandelbauer, A. IR Spectroscopy: Suitable Method for Determination of Curing Degree and Crosslinking Type in Melamine–Formaldehyde Resins. *J Appl Polym Sci* **2019**, *136*, 47691.
(73) Berthon-Fabry, S.; Hildenbrand, C.; Ilbizian, P. Lightweight Superinsulating Resorcinol-Formaldehyde-APTES Benzoxazine Aerogel Blankets for Space Applications. *European Polymer Journal* **2016**, *78*, 25–37.
(74) Rasines, G.; Lavela, P.; Macías, C.; Zafra, M. C.; Tirado, J. L.; Ania, C. O. On the Use of Carbon Black Loaded Nitrogen-Doped Carbon Aerogel for the Electrosorption of Sodium Chloride from Saline Water. *Electrochimica Acta* **2015**, *170*, 154–163.

(75) Cançado, L. G.; Takai, K.; Enoki, T.; Endo, M.; Kim, Y. A.; Mizusaki, H.; Jorio, A.; Coelho, L. N.; Magalhães-Paniago, R.; Pimenta, M. A. General Equation for the Determination of the Crystallite Size La of Nanographite by Raman Spectroscopy. *Appl. Phys. Lett.* **2006**, *88*, 163106.
(76) Rasines, G.; Lavela, P.; Macías, C.; Zafra, M. C.; Tirado, J. L.; Ania, C. O. Mesoporous Carbon Black-Aerogel Composites with Optimized Properties for the Electro-Assisted Removal of Sodium Chloride from Brackish Water. *Journal of Electroanalytical Chemistry* **2015**, *741*, 42–50.
(77) Jaouen, F.; Lefèvre, M.; Dodelet, J.-P.; Cai, M. Heat-Treated Fe/N/C Catalysts for O2 Electroreduction: Are Active Sites Hosted in Micropores? *J. Phys. Chem. B* **2006**, *110*, 5553–5558.
(78) Jia, Q.; Ramaswamy, N.; Tylus, U.; Strickland, K.; Li, J.; Serov, A.; Artyushkova, K.; Atanassov, P.; Anibal, J.; Gumeci, C.; Barton, S. C.; Sougrati, M.-T.; Jaouen, F.; Halevi, B.; Mukerjee, S. Spectroscopic Insights into the Nature of Active Sites in Iron–Nitrogen–Carbon Electrocatalysts for Oxygen Reduction in Acid. *Nano Energy* **2016**, *29*, 65–82.
(79) Mineva, T.; Matanovic, I.; Atanassov, P.; Sougrati, M.-T.; Stievano, L.; Clémancey, M.; Kochem, A.; Latour, J.-M.; Jaouen, F. Understanding Active Sites in Pyrolyzed Fe–N–C Catalysts for Fuel Cell Cathodes by Bridging Density Functional Theory Calculations and 57Fe Mössbauer Spectroscopy. *ACS Catal.* **2019**, *9*, 9359–9371.
(80) Goenaga, G. A.; Roy, A. L.; Cantillo, N. M.; Foister, S.; Zawodzinski, T. A. A Family of Platinum Group Metal-Free Catalysts for Oxygen Reduction in Alkaline Media. *Journal of Power Sources* **2018**, *395*, 148–157.
(81) Shinagawa, T.; Garcia-Esparza, A. T.; Takanabe, K. Insight on Tafel Slopes from a Microkinetic Analysis of Aqueous Electrocatalysis for Energy Conversion. *Sci Rep* **2015**, *5*, 13801.
(82) Primbs, M.; Sun, Y.; Roy, A.; Malko, D.; Mehmood, A.; Sougrati, M.-T.; Blanchard, P.-Y.; Granozzi, G.; Kosmala, T.; Daniel, G.; Atanassov, P.; Sharman, J.; Durante, C.; Kucernak, A.; Jones, D.; Jaouen, F.; Strasser, P. Establishing Reactivity Descriptors for Platinum Group Metal (PGM)-Free Fe–N–C Catalysts for PEM Fuel Cells. *Energy & Environmental Science* **2020**, *13*, 2480–2500.
(83) Kumar, K.; Dubau, L.; Mermoux, M.; Li, J.; Zitolo, A.; Nelayah, J.; Jaouen, F.; Maillard, F. On the Influence of Oxygen on the Degradation of Fe-N-C Catalysts. *Angewandte Chemie* **2020**, *132*, 3261–3269.
(84) Jaouen, F.; Goellner, V.; Lefèvre, M.; Herranz, J.; Proietti, E.; Dodelet, J. P. Oxygen Reduction Activities Compared in Rotating-Disk Electrode and Proton Exchange Membrane Fuel Cells for Highly Active FeNC Catalysts. *Electrochimica Acta* **2013**, *87*, 619–628.
(85) Liu, S.; Deng, C.; Yao, L.; Zhong, H.; Zhang, H. The Key Role of Metal Dopants in Nitrogen-Doped Carbon Xerogel for Oxygen Reduction Reaction. *Journal of Power Sources* **2014**, *269*, 225–235.